Coupling of magnetism, crystal lattice, and transport in EuCuP and EuCuAs

Andrew F. May ⬤,[*] Eleanor M. Clements ⬤, Heda Zhang, Raphael P. Hermann ⬤, Jiaqiang Yan ⬤, and Michael A. McGuire ⬤

Materials Science and Technology Division, Oak Ridge National Laboratory, Oak Ridge, Tennessee 37831, USA

EuCuP and EuCuAs are members of a family of materials with candidates for realizing magnetically tuned electronic topology. In this work, the magnetic phase transitions and magnetoelastic coupling of EuCuP and EuCuAs have been investigated. Around the Curie temperature, the thermal expansion coefficient and specific-heat capacity of EuCuP are found to have two closely spaced features, at approximately 30 and 31.3 K, which may indicate a cascading magnetic transition or perhaps an electronic transition closely coupled to the magnetic ordering. The zero-field magnetoelastic coupling appears to be stronger in EuCuP than in EuCuAs, and field-dependent measurements suggest this is due to the dominant ferromagnetic interaction in EuCuP as opposed to antiferromagnetic order in EuCuAs below $T_{\mathrm{N}} = 13.5$ K. Thermal expansion is anisotropic around T_{N} in EuCuAs, with a maximum expansion along [001] occurring above T_{N} prior to a stiffening of this c-axis component on cooling through T_{N}; the expansion of the basal plane has a lambda-like peak centered slightly above T_{N}. Matching these behaviors, the ac susceptibility data for EuCuAs suggest the presence of strong ferromagnetic correlations above T_{N} in the vicinity where the c-axis expansion peaks. Both compounds possess similar electrical and thermoelectric transport behaviors, with short-range magnetic order likely playing an important role above T_{C} or T_{N}. Transport properties suggest these are predominantly hole doped due to intrinsic defects, and narrow-gap semiconducting or semimetallic behavior may be achievable if the underlying defects can be tuned.

I. INTRODUCTION

Understanding the coupling of electronic topology and magnetic ordering is a central theme of many current efforts in materials physics. Naturally, the symmetry of the host lattice also plays a vital role, and magnetism can impact the global symmetry through magnetoelastic coupling and via long-range magnetic order that may or may not break time-reversal symmetry. In turn, the ability to change the magnetic order via an applied magnetic field provides a route to tune electronic topology, which is essential for both fundamental studies as well as for understanding how future applications may exploit these electronic responses. A few material families have emerged as prime candidates for fundamental studies and the best ones generally contain intrinsic magnetism, such as in $MnBi_2Te_4$ [1–7], $Co_3Sn_2S_2$ [8–11], and pnictide-containing Zintl materials such as $EuIn_2As_2$ [12–17], $EuCd_2As_2$ [18–21], $EuMnBi_2$ [22–25], and $EuSn_2P_2$ [26,27].

The EuMPn compounds with $Pn =$ P, As, Sb, Bi and $M =$ Cu, Ag, Au have become of interest lately for their potential to exhibit magnetic tuning of electronic topology, which was motivated by the topological nonmagnetic alkaline-earth-metal analogs [28–34]. This is not surprising, as simple electron counting yields a charge balanced system with $Eu^{2+}M^{1+}Pn^{3-}$ and one can perhaps consider this as a Zintl-like compound where a covalent $(MPn)^{2-}$ network is supported by charge donation from the layer of Eu^{2+} [35].

Small band gaps are common in these types of Zintl phases and the potential for band inversion exists [31], such as found in the trigonal $CaAl_2Si_2$-type Zintl materials like $EuCd_2As_2$. Within EuMPn materials, EuAgAs provides a nice example, with calculations predicting Dirac points in the paramagnetic phase that evolve based on the magnetic order to potentially produce a variety of topologically nontrivial electronic states [36]. This bears a resemblance to behavior of the Zintl phase $EuIn_2As_2$, an axion insulator for which the magnetic structure impacts the electronic topology and surface states [13–17].

Here we focus on the understudied compounds EuCuP and EuCuAs [37], which are members of a large family of compounds forming in the BeZrSi structure type (space group $P6_3/mmc$ No. 194). The hexagonal crystal structure contains a triangular lattice of Eu^{2+} ($S = \frac{7}{2}$, $L = 0$) that is separated by honeycomb CuP (CuAs) sheets as shown in Fig. 1. Similar Eu-Eu distances are observed within and between the triangular layers, with the shortest distance being between triangular lattices and not within. The crystal structure is an ordered variant of the Ni_2In structure type, which has two Ni sublattices that order chemically in the ternary compounds. The Ni_2In structure is a derivative of the hexagonal NiAs structure type that is formed by filling the empty trigonal prismatic site at $(\frac{1}{3}, \frac{2}{3}, \frac{3}{4})$. It is worth noting that the ternary structure is similar to that of the skyrmion-hosting material Gd_2PdSi_3 [38–42], which has the same fundamental structure but with Pd-Si ordering within the honeycomb network that leads to structural complexities [43]. Rare-earth materials like this (nominally spin-only moments, with or without geometric frustration) have become platforms for understanding how competing interactions can
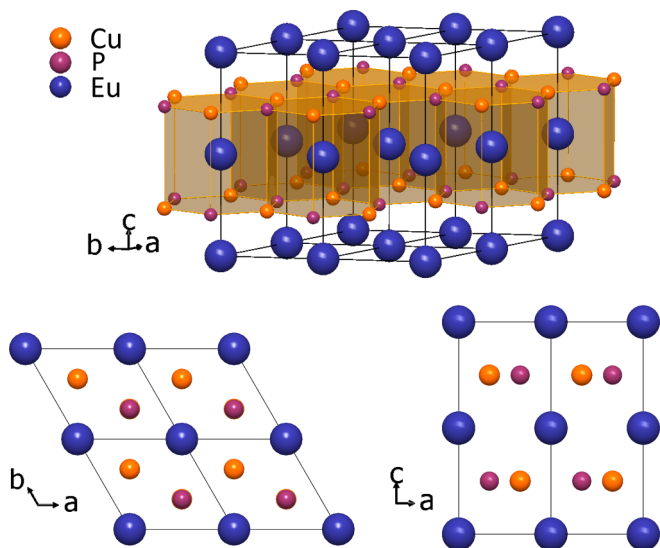
---

*mayaf@ornl.gov

FIG. 1. Crystal structure of EuCuP with triangular lattices of divalent Eu atoms separated by honeycomb Cu-P networks; As substitutes for P to form isostructural EuCuAs. In both materials, the shortest Eu-Eu distance is between the triangular lattices (along [001]) and equal to $\frac{1}{2}$ of the c-axis lattice parameter; lattice parameters obtained from x-ray diffraction data at ambient temperature for EuCuP are $a = 4.1205(4)$ Å and $c = 8.1939(9)$ Å, and for EuCuAs the refined values are $a = 4.2530(1)$ Å and $c = 8.2614(2)$ Å. The Eu-Eu distances along [001] and [100] are close to equal in EuCuP but are nearly 3% different in EuCuAs.

stabilize complex, perhaps topological, spin structures in systems that are globally centrosymmetric [44–47]. This provides further motivation to understand the nature of the magnetism and its connection to the crystal lattice in EuMPn materials.

The magnetic moments in EuMPn with $M =$ Cu, Ag, Au order in various configurations depending on the nature of the pnictide [37,48]: the phosphides are ferromagnetic, the antimonides are antiferromagetic, and the behavior of the arsenides depends on the transition metal. For the Cu-based compounds, EuCuP is a ferromagnet ($T_C \approx 31$ K) [49,50], EuCuAs is an easy-plane antiferromagnet ($T_N \approx 14$ K), and EuCuSb possesses collinear antiferromagnetic (8.5 K) and helic order (6 K) [51]. A more-detailed study of EuCuP is warranted to determine if there is evidence of a more complex magnetic ground state given the previous characterization as an anomalous ferromagnet [49]; comparisons to EuCuAs are drawn to facilitate this inspection and determine if this antiferromagnetic phase appears more complex than previous literature suggests [52].

In this work, we examine the coupling of the magnetism, crystal lattice, and transport properties of EuCuP and EuCuAs by characterizing flux-grown single crystals. We find that a stronger magnetoelastic coupling exists in EuCuP as compared to EuCuAs, as exemplified by both dilatometry and thermal conductivity measurements. All of the crystals are found to be p-type conductors, with thermoelectric transport properties similar to those of heavily doped semiconductors (Hall carrier densities on the order of 10^{20}–10^{21} cm^{-3}). In EuCuP, two features are observed in the thermal expansion and specific heat across T_C, though Mössbauer spectroscopy

does not resolve large changes in the europium hyperfine parameters. Many of the observed properties in EuCuP bear a striking similarity to those in the Weyl semimetal EuB$_6$ where short-range order above T_C has been linked to electronic phase separation that strongly impacts the transport properties and lattice response [53–55]. Future studies to understand the electronic topology of this family will benefit from an effort to control the intrinsic defect concentrations since p-type conduction is consistently observed and samples of EuCuP from a single-crystal growth had significant variations in Hall density and resistivity.

II. METHODS

Crystals of EuCuP, EuCuAs, CaCuP, and CaCuAs were grown from a Sn flux. The growths were performed in Al$_2$O$_3$ crucibles of the Canfield type (Al$_2$O$_3$ frit-disc filters [56]) that were sealed under vacuum inside fused silica tubing. High-purity elements were utilized in shot (Cu) or pieces (P,As) with the Eu being sourced from Ames Laboratory and Ca obtained in dendritic form from Alfa Aesar. Reactions, at compositions such as 7EuCuP:93Sn, were loaded in a glovebox and transferred to the vacuum line under inert gas as described in Ref. [57]. Heating rates were limited to 100 °C/h at most, and the initial growths utilized a first dwell at 600 °C until the reactions with arsenic and these elements were tested to minimize safety concerns. Following homogenization at 1000 °C for at least 12 h, the furnaces were cooled to a minimum of 500 °C and the excess flux was separated from the crystals using a centrifuge. Crystals of EuCuP were obtained from growths terminated up to 800 °C and no significant difference in the magnetic behaviors was observed. We generally obtained larger crystals for EuCuAs compared to EuCuP, though attempts were not made to optimize the growths for crystal size since the 1–5 mm crystals are large enough for all desired measurements.

X-ray diffraction was performed using a PANalytical X'Pert Pro MPD with a Cu $K\alpha_1$ ($\lambda = 1.5406$ Å) incident beam monochromator. An Oxford PheniX closed-cycle helium cryostat was utilized to obtain diffraction data on EuCuP down to $T = 15$ K. Rietveld refinements were performed using the program FULLPROF [58]. These phases were not observed to be air sensitive, even when ground to powder. Crystals were examined in a Hitachi TM-3000 scanning electron microscope equipped with a Bruker Quantax 70 EDS detector system. These measurements, as well as the magnetization and initial transport measurements, clearly revealed the existence of flux (Sn) inclusions within the crystals. Crystals were thinned by grinding on silicon carbide paper in an effort to avoid the presence of Sn inclusions during final transport measurements. Aside from the Sn flux, no additional impurity phases were detected by x-ray diffraction.

Physical property measurements were performed in Quantum Design cryostat systems using standard practices and measurement options, including large-pulse specific-heat measurements to obtain dense data spacing across the phase transitions. Dilatometry experiments were performed using Quantum Design's fused silica capacitive cell [59]; low-T data were collected using a rate of 0.2 K per minute, which was deemed reasonable based on the lack of thermal

hysteresis observed on warming or cooling as well as the agreement of characteristic temperatures for EuCuP as compared to specific-heat measurements where the sample temperature is perhaps better defined. Isothermal dilation as a function of field was measured using 10 Oe/s ramp rates. Dilation was measured on crystals that were mechanically shaped to the correct size, using a fused silica shim for [001] expansion. Hall effect measurements were also performed on thinned samples. The magnetic behaviors of crystals that were ground on polishing papers were the same as those obtained on as-grown crystals, with the exception being the impact of demagnetizing effects that are dependent on the sample geometry and can be large in these materials with large magnetic moments.

The thermal transport option (TTO) was utilized to measure the thermoelectric transport properties of EuCuP and EuCuAs. Crystals of similar sizes were utilized to minimize the impacts of systematic errors on the comparisons made; for EuCuP the separation between leads was 3.61 mm with a cross-sectional area of 1.02 mm^2, while for EuCuAs the lead separation was 3.15 mm with a cross-sectional area of 1.21 mm^2. For EuCuAs, the minimum period was changed to 100 s to avoid an artifact in the region of the maximum κ, whereas for EuCuP the minimum period was left at 30 s in the Quantum Design MULTIVIEW software. A home-built system [60] was used to obtain the thermal conductivity and Seebeck coefficient of CaCuAs due to the small size of those crystals. The home-built system utilizes small cernox thermometers that are affixed to the sample using gold wires via silver paint (Dupont 4929N). Heat is supplied at one end of the sample and the other end is attached to a copper heat sink by Ag paint. The Seebeck coefficient is measured by obtaining the voltage (via Manganin wires) in the direction of the temperature gradient. A steady state condition is acquired and the Seebeck coefficient is obtained from the voltage differences recorded under a temperature gradient, with any voltage occurring during an isothermal state being removed so that only the portion proportional to the temperature difference contributes. Measurements are performed using Keithley instruments (K2182 Nanovolt meter) via a MATLAB script.

Transmission europium-151 Mössbauer spectra were recorded on 68 mg/cm^2 powder of EuCuP placed in a Janis SHI-850 closed cycle cryostat; the powder was obtained by grinding crystals. A 40-mCi room-temperature ^{151}SmF3 source was used on a Wissel GmbH drive operating in the ± 50 mm/s velocity range, calibrated with α-iron foil. The isomer shift is relative to the SmF$_3$ source.

III. RESULTS AND DISCUSSION

A. Structural characterization

X-ray diffraction and scanning electron microscopy with energy dispersive spectroscopy were used to assess the phase purity and crystal structure of the EuCuP and EuCuAs crystals. X-ray diffraction data are consistent with the expected BeZrSi structure type for all compounds studied here, as illustrated by the Rietveld refinement shown in Fig. 2 for EuCuP. We examined the temperature dependence of the lattice for EuCuP below T_C down to $T = 15$ K using a laboratory
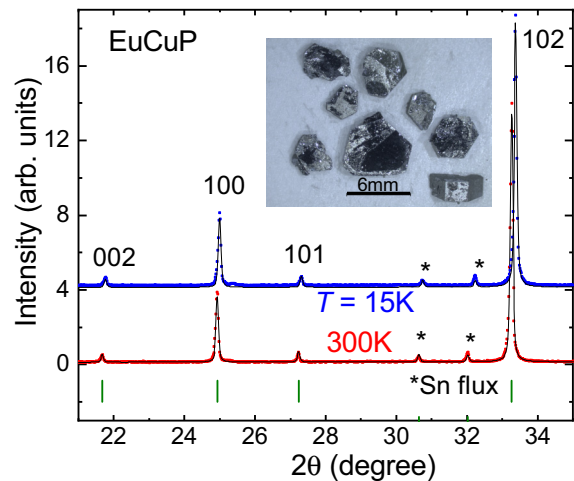

FIG. 2. Powder x-ray diffraction data for pulverized EuCuP at $T = 15$ and 300 K. Rietveld refinements in the hexagonal space group No. 194 (black lines) demonstrate that the lattice symmetry does not change upon the magnetic ordering transition at ≈ 31 K. The inset is a picture of EuCuP crystals; these crystals were grown in an alumina crucible (5 mL) while cooling at 1 K/hr to an ultimate temperature of 700 °C.

cryostat. These measurements demonstrated that the crystal symmetry of EuCuP does not change in response to the magnetic transition, and thus the triangular lattice of Eu moments is preserved. This is perhaps not surprising since the spins are believed to orient along the c axis in the ferromagnetic (or nearly ferromagnetic) spin configuration. There is a large contraction upon cooling below T_C and this strong magnetoelastic coupling in EuCuP was previously studied with dilatometry measurements [49]; we have further explored this effect with dilatometry and thermal transport as discussed below. Consistent with the dilatometry data, x-ray diffraction reveals that the contraction upon cooling through T_C is greatest along the c axis in EuCuP. At 15 K, the refined lattice parameters are $a = 4.1097(3)$ Å and $c = 8.1598(9)$ Å, while at 300 K $a = 4.1205(4)$ Å and $c = 8.1939(9)$ Å for EuCuP; the powder for x-ray diffraction was obtained by grinding crystals.

Material properties are expected to be three dimensional because the shortest Eu-Eu distance is along the c axis and not within the triangular lattice (distance ratio = 0.994 in EuCuP and 0.972 in EuCuAs). The three-dimensional nature of the material is also observed in the crystals themselves, which are blocky plates that do not cleave well (see inset of Fig. 2).

When considering the structure of these materials, it is worth highlighting that the transition metal electron count appears to dictate the structure of these and related compositions. For instance, EuMPn compounds with $M =$ Ni, Pt, Pd exist with minor structural differences being atomic shifts in the (MPn) layers that lead to reduced symmetry and/or puckering of the honeycomb networks. Importantly, these structural changes are also coupled to changes in the Eu valence, with compounds such as EuPtP displaying temperature-dependent mixed valency (Eu^{2+}/Eu^{3+}) [61–63]. However, Mössbauer studies have revealed homogeneous
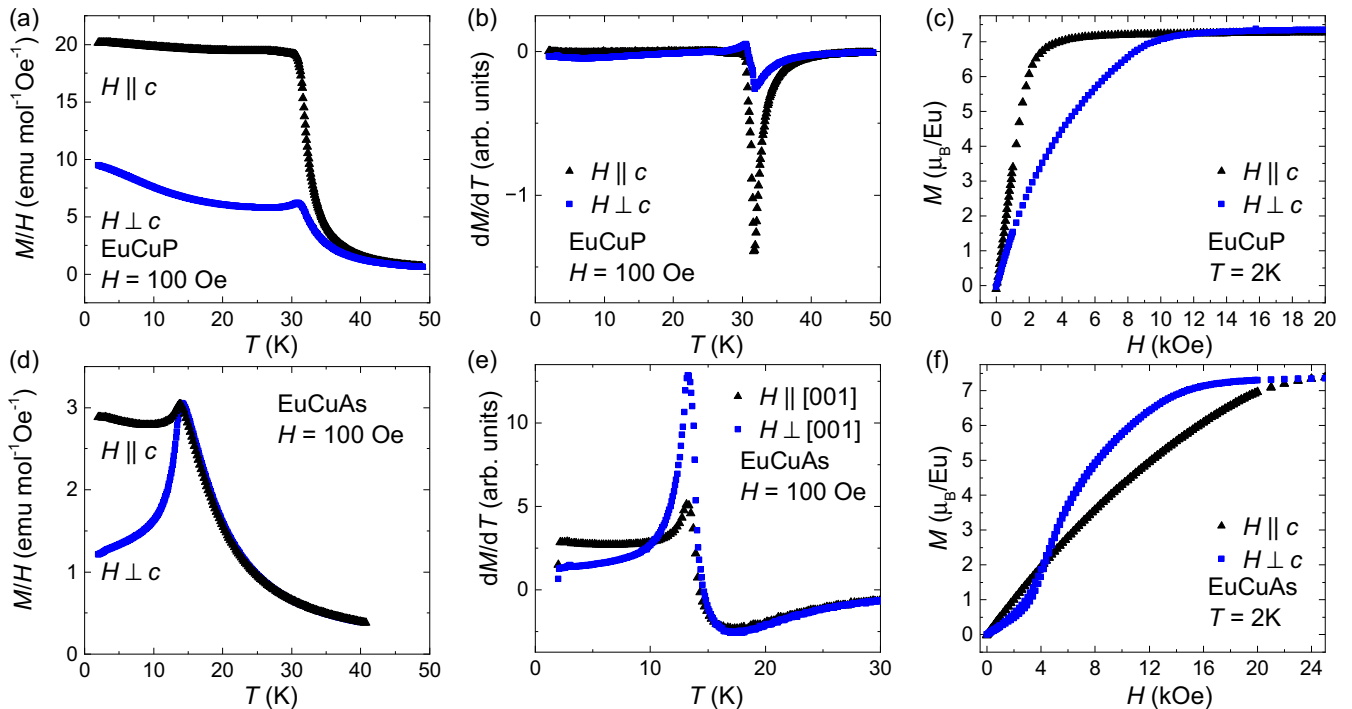
FIG. 3. The dc magnetization data for EuCuP (upper row) and EuCuAs (lower row). (a), (d) Temperature-dependent magnetization obtained upon cooling in an applied field and (b), (e) the corresponding dM/dT data. (c), (f) Isothermal magnetization data revealing the easy-axis [001] anisotropy of EuCuP and the easy-plane antiferromagnetic configuration of EuCuAs is observed by the metamagnetic transition when the field is applied perpendicular to the c axis.

divalent Eu in the $M =$ Cu, Ag, Au compounds [62]. We have also performed Mössbauer spectroscopy on pulverized EuCuP crystals and the spectra are indeed consistent with divalent Eu with a very minor Eu^{3+} believed to be caused by surface oxidation. In addition, the low-T spectra of EuCuP are consistent with a single Eu site as expected from the diffraction data collected at 15 K.

B. Magnetic properties

Magnetic properties of EuCuP and EuCuAs have been reported based on anisotropic magnetization measurements of single crystals, and more limited magnetization data were reported for polycrystalline samples [37,49,50,52]. In this work, the magnetic properties are explored in further detail through ac susceptibility, specific-heat, and dilatometry measurements. To introduce the general behavior, Fig. 3 summarizes the dc magnetization data for our crystals and these results are consistent with the existing literature. The observed ordering temperatures are $T_C \approx 31$ K in EuCuP and $T_N \approx 14$ K for EuCuAs. More quantitatively, for 100 Oe applied along [001], dM/dT has a large negative peak centered at 31.7 K for EuCuP, while in EuCuAs there is a positive peak at 13.2 K (decrease in M on cooling due to magnetic order); in the correlated paramagnetic phase, dM/dT has a broad negative peak centered near 15.5 K for EuCuAs. At high temperatures, Curie-Weiss behavior is observed fitting to a Curie-Weiss model reveals a positive Weiss temperature in both materials, corresponding to dominant ferromagetic interactions [48].

EuCuP has predominant easy-axis [001] magnetic anisotropy as illustrated in Fig. 3(c). This anisotropy begins to develop above T_C as the correlations increase and short-range order may develop. The nonlinearity of $M(H)$ at $T = 2$ K for $H \perp c$ [Fig. 3(c)] is not easily understood in a simple ferromagnetic model and does not appear to be an artifact of sample misalignment based on comparisons of multiple measurements. The data in Fig. 3(c) were obtained on a crystal of EuCuP that was polished so that geometry-determined demagnetization factors would be approximately equal for both orientations and the intrinsic anisotropy is thus qualitatively reflected in the results. In-plane anisotropy was not observed between the $H \parallel$ [100] and [110] directions, which is slightly different than the data in Ref. [49]; demagnetization effects may be the source for this discrepancy. The demagnetization effects have not been corrected for in Fig. 3(c), which would cause the $M(H)$ curves to shift to lower fields if the applied field was converted into an internal field.

In antiferromagnetic EuCuAs, the preferred moment orientation is inverted relative to EuCuP, with the moments confined to the basal plane at zero field. This easy-plane behavior is evidenced by the metamagnetic transition for $H \perp c$ observed near $H = 4$ kOe at $T = 2$ K as shown in Fig. 3(f). The anisotropy is also consistent with the temperature-dependent magnetization data. As seen in Fig. 3(d), the magnetization below T_N decreases upon cooling when the field is applied within the basal plane whereas it is relatively independent of temperature when the field is applied along the c axis.
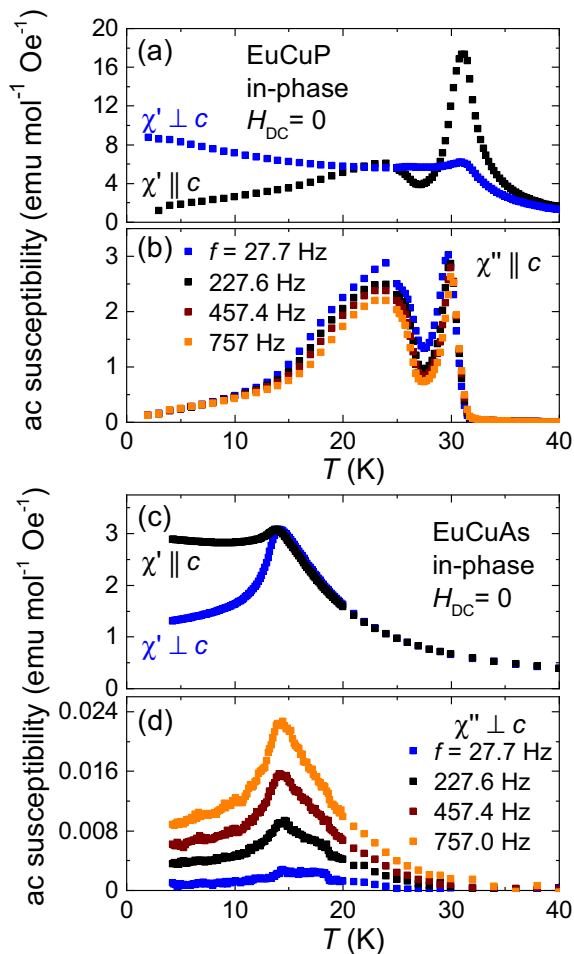
FIG. 4. The ac magnetic susceptibility data for (a), (b) EuCuP and (c), (d) EuCuAs with zero applied dc magnetic field. (a), (c) Present the anisotropic in-phase contribution χ' and (b), (d) display the the out-of-phase χ'' for the easy-moment orientations as labeled. The ac driving amplitude was 2 Oe and data in (a) and (c) are for $f = 227$ Hz.

Ac magnetic susceptibility measurements provide a different perspective than dc measurements. Data for EuCuP and EuCuAs are shown in Fig. 4. The ac susceptibility is presented utilizing the in-phase (χ') and out-of-phase (χ'') contributions. While the in-phase component at low frequencies f is closely related to the dc susceptibility, the out-of-phase component originates in losses from spin dynamics such as domain movements and electronic effects in high-conductivity metals [64]. The ac susceptibility of antiferromagnetic materials is thus dominated by χ' with χ'' typically zero (or nearly so). By contrast, ferromagnetic materials can have a large χ'' below the Curie temperature as domains form and are mobile. In this sense, the ac susceptibility provides a tool that is complementary to dc measurements, which are dominated by the largest induced magnetization. In addition, ac measurements can be performed with zero dc magnetic field and small oscillating fields, making them useful when data are being compared to other zero-field probes such as

specific-heat capacity, Mössbauer spectroscopy, or neutron diffraction.

Ac magnetic susceptibility data in Fig. 4 were collected in the absence of a dc magnetic field using the same crystals as for the dc data shown in Fig. 3. χ' for in-plane and out-of-plane orientations of EuCuP are shown in Fig. 4(a). The dominant feature is a peak in χ' near T_C, which is expected for a ferromagnet, and the peak is most significant for the [001] easy axis. We use this maximum to define $T_C = 31.25$ K. As expected, there is a corresponding peak just below T_C in the out-of-phase component χ'' [Fig. 4(b)]. In addition, there is a second peak in both χ'' and χ'' near 26 K with the exact temperature depending on orientation. This behavior is likely related to an evolution of the domains and perhaps hints at a subtle evolution of the magnetic anisotropy. As discussed below, there are no anomalies observed in the specific-heat capacity or thermal expansion near 26 K in EuCuP, which suggests that this feature is not related to a phase transition since dilatometry is very sensitive to magnetization changes in this system. There is potentially a very minor frequency dependence for the peak near T_C in EuCuP. Both χ' and χ'' are peaked at slightly higher T for the highest frequency compared to the lowest frequency (behavior not shown for χ'); the difference is subtle because the peak is rather broad and the maximum values differ by 0.25 K which was the step size of this measurement. The in-phase contribution peaks at 31.25 K for $f = 757$ Hz, which is 1.25 K above the peak in the out-of-phase contribution. The characteristic temperature of the anomaly near 26 K does not have a clear frequency dependence. The small frequency dependence of the peak at T_C does not appear to be an artifact since a similar frequency dependence was not observed for EuCuAs. While the out-of-phase contribution is large, the frequency dependence is extremely weak and the results (ac and dc) are generally not consistent with a spin (or cluster) glass.

The ac susceptibility data for EuCuAs are shown in Figs. 4(c) and 4(d). Upon close inspection, it is seen that the magnetic susceptibility of EuCuAs (ac and low-field dc) reaches a maximum at slightly lower temperatures when the susceptibility is measured along the c axis (a difference of about 0.25 K). For both orientations, the temperature derivative of the in-phase contribution ($d\chi'/dT$) peaks at 13.3 K (same T for peak of $d\chi'T/dT$). This peak in the derivative affords a definition of $T_N = 13.3$ K, which is in reasonable agreement with the specific-heat data. Within resolution caused by data-point spacing, a similar anisotropy in the maximum susceptibility was not observed in EuCuP. The susceptibility becomes anisotropic above T_C in EuCuP, a behavior not observed in EuCuAs except right at the position of the maximum susceptibility values.

Interestingly, the out-of-phase contribution peaks above the ordering transition in EuCuAs. This is most dramatic for the lowest frequencies, where a shoulder can be seen around 18 K. This is rather unusual, and may point to short-range precursors existing above T_N, and the link to an out-of-phase ac contribution would perhaps suggest these are ferromagnetic in nature. The value of the in-phase contribution is similar to the dc M/H data in Fig. 3(d) due to the antiferromagnetic nature of EuCuAs, with the out-of-phase contribution being much smaller (less than 1%).
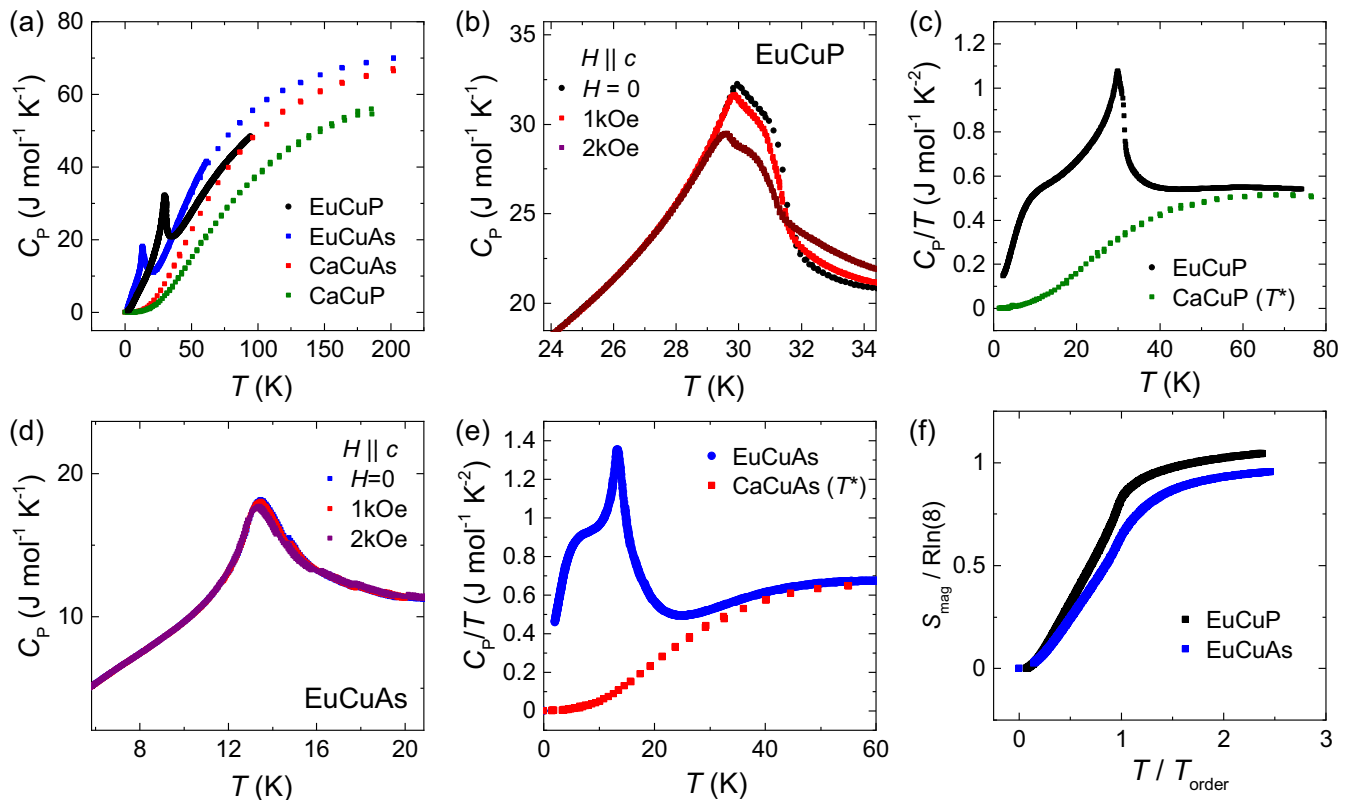
FIG. 5. (a) Specific-heat capacity of EuCuP, EuCuAs, and nonmagnetic counterparts CaCuP and CaCuAs. (b), (c) Close inspection of the data for EuCuP around its Curie temperature, similar to those in (d) and (e) for EuCuAs around its Néel temperature. (f) Magnetic entropy esitmate from integration of data in (c) and (e) plotted versus normalized temperature where T_{order} is T_C for EuCuP and T_N for EuCuAs. The minor quantitative difference in how the integrated entropy approaches that expected for the $S = \frac{7}{2}$ ion could be linked to the quality of the nonideal phonon backgrounds utilized.

C. Specific heat

Specific-heat capacity (C_P) measurements were used to examine the magnetic phase transitions, for instance, to search for evidence of multiple transitions or discontinuities. Anomalies are observed near the magnetic transitions, as illustrated in Fig. 5(a), consistent with the expectations of long-range magnetic order. An anomaly is not observed in EuCuP near 25 K, the temperature where additional peaks were observed in the ac susceptibility data. In both EuCuP and EuCuAs, there is a prominent low-T shoulder far below the magnetic transition when the data are viewed as C/T. This feature is expected from mean field theory, as discussed in Ref. [65], and thus not believed to be an indication of an additional phase transition or some complex evolution of the lattice and magnetic structure.

To obtain an estimate of the magnetic entropy by integrating C_P/T, crystals of nonmagnetic CaCuP and CaCuAs were grown and specific heat capacity data on these samples were collected for use as phononic backgrounds. Due to the large differences in atomic masses of Ca and Eu, the elastic properties are expected to vary substantially and thus these are not ideal phonon backgrounds. These trends are observed as a shift of the $C_P(T)$ curves such that a higher specific heat is reached at a given intermediate temperature (say 100 K) for the materials containing heavier elements [see Fig. 5(a)], which is typically driven by the lower Debye

temperature in lattices with higher molecular weights. For instance, well above the magnetic transitions, the specific heat of EuCuAs is larger than that of EuCuP and these C_P values are still rising towards the Dulong-Petite value of 3R/atom (74.8 J mol^{-1} K^{-1}). To utilize the C_P/T data of CaCuP and CaCuAs as nonmagnetic baselines, a temperature-mass scaling was performed to compute a new effective temperature T^* using, for example, in the case of CaCuP-EuCuP analysis, $T^* = T (M_{CaCuP}/M_{EuCuP})^{\frac{1}{2}}$ where M is the molecular weight [65]. The scaled data are shown in Figs. 5(c) and 5(e). This approach provides a semiquantitative estimate of the magnetic entropy for EuCuP and EuCuAs, the result of which is shown in Fig. 5(f) where the evolution versus relative temperature is similar for these two materials. The integrated entropy is plotted as a fraction of the value expected for the $S = \frac{7}{2}$ moment in the paramagnetic phase.

Near the Curie temperature, the specific heat of EuCuP has a broadened anomaly that rises to a peak near 31 K. Closer inspection reveals a slight shoulder near 31.5 followed by the peak and downturn below 30 K. This behavior was confirmed through measurements on several crystals, and while present in all crystals the fine detail of the features varied between different crystals (see Fig. 14 in the Appendix); the crystal used for the data in Fig. 5 was also used during dilatometry measurements for consistency. Measurements were performed in applied fields ($H \parallel c$) to observe how these features evolved

and this proved useful in isolating these anomalies as distinct features. As observed in Fig. 5(b), it becomes easy to observe deviations from a simple lambda anomaly with increasing field, and the high-T shoulder becomes more prominent at 1 kOe and by 2 kOe the peak is generally truncated but with texture that remains. Interestingly, both characteristic features are suppressed slightly by the applied fields, though some entropy is drawn to higher temperatures as well; at higher fields, the feature generally broadens with increasing entropy pulled to higher temperatures. These features suggest something more complicated than a singular ordering event at T_C, and perhaps there are two magnetic transitions near T_C in zero field. By contrast, the behavior of C_P in EuCuAs is rather simple with a singular anomaly centered near 13.5 K; there is a lack of field dependence at modest fields for $H \parallel c$ as expected from the magnetization data and specific-heat data for $H \perp c$ were not collected.

D. Lattice expansion

Dilatometry is extremely sensitive to small lattice changes and can detect phase transitions or other anomalies that are difficult to probe with other laboratory characterization techniques [66]. Dilation data ($\Delta L/L_0$ in parts per million, ppm) were collected in various configurations to probe the anisotropic lattice expansion. The temperature derivative of the dilation is the thermal expansion coefficient α presented in ppm/K. A peak in the thermal expansion coefficient generally indicates a continuous phase transition. The field derivative of dilation during isothermal measurements is the magnetostriction coefficient λ reported in ppm/Oe, and corresponding dilation plots establish L_0 as the value at zero field.

Thermal expansion data for EuCuP have been reported in Ref. [49], and the qualitative trends near T_C are consistent with those reported here. However, by examining the behavior around T_C more closely, the current results reveal a more complex scenario than previously reported. In addition, data for EuCuAs and CaCuAs have been included.

The temperature-dependent dilation data for EuCuP, Eu-CuAs and CaCuAs are shown in Fig. 6(a). The relative length change is similar for all compounds, with a small anisotropy and the c axis contracting fastest on cooling. The expansion is most anisotropic in EuCuP and the change upon cooling through the magnetic transition is also most significant in EuCuP. The a-axis expansions of EuCuAs and CaCuAs are very similar at temperatures well above T_N, while the c-axis expansion of all compounds is quite similar above ≈ 100 K (subtle differences exist).

Interesting behavior is observed near the ordering transitions in both EuCuP and EuCuAs, which is best observed via the thermal expansion coefficient. As shown in Fig. 6(b), α of EuCuP has a very dramatic peak for c-axis expansion, but the anomaly contains two characteristic temperatures (a shoulder at $T_C = 31.25$ K and a peak at 30 K for $H = 0$). Expansion in the basal plane is much less significant, and a truncated peak in α is bracketed by these two characteristic temperatures. This two-feature behavior was not reported in Ref. [49] where only the dilation data were presented. The behavior of $\alpha_{[001]}$ is similar to that of ferromagnetic semimetal EuB$_6$ near its Curie temperature, where the higher-temperature feature has
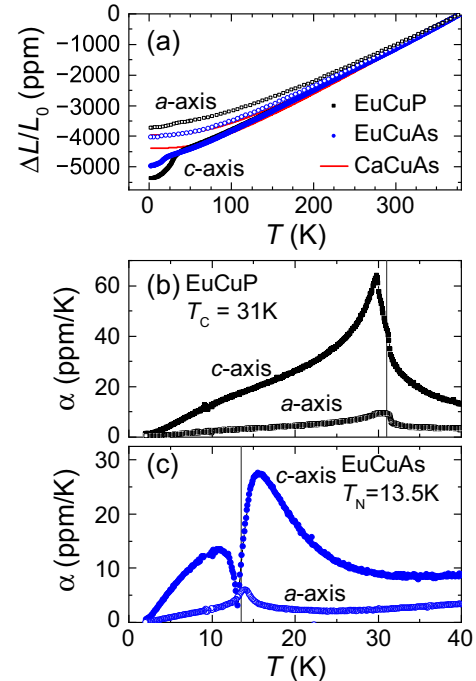

FIG. 6. Dilation data for EuCuP, EuCuAs, and nonmagnetic CaCuAs. (a) Dilation data showing the relative contraction upon cooling, with L_0 values obtained at 380 K. (b), (c) Thermal expansion coefficients around the magnetic transitions in EuCuP and EuCuAs with orientations listed. Vertical lines in (b) and (c) represent the magnetic ordering temperatures based on specific heat data.

been associated with the formation of short-range magnetic clusters and the sharp peaks in α and C_P were associated with formation of long-range order [54].

The lattice expansion of EuCuAs is also anisotropic near its magnetic ordering transition, but in a very different manner than in EuCuP. In EuCuAs, a maximum α occurs at 14 K for in-plane expansion, while along the c axis there is a maximum further above T_N at 15.7 K and a sharp minimum at 13.1 K. The broad maximum at ≈ 11 K is likely the result of $\alpha \rightarrow 0$ as $T \rightarrow 0$, forcing a maximum to occur after the lattice behavior normalizes following the sharp minimum below T_N for $L \parallel [001]$. These results reveal a strong impact of the magnetization on the lattice starting from well above the ordering temperatures in both EuCuP and EuCuAs, consistent with the observation of magnetic correlations in the specific-heat data well above the ordering temperatures.

The magnetoelastic coupling in EuCuP and EuCuAs was further analyzed via field-dependent dilation measurements. We first consider the impact of an applied field on the thermal expansion coefficient of EuCuP in Fig. 7(a). An applied field along the easy axis of EuCuP is found to suppress both the high-T shoulder and the prominent peak in the thermal expansion coefficient near the Curie temperature. It is worth emphasizing that the qualitative evolution of the thermal expansion coefficient with applied field is similar to that of the specific-heat capacity. This suppression of features by an applied field appears more reminiscent of an antiferromagnet than of a ferromagnet.
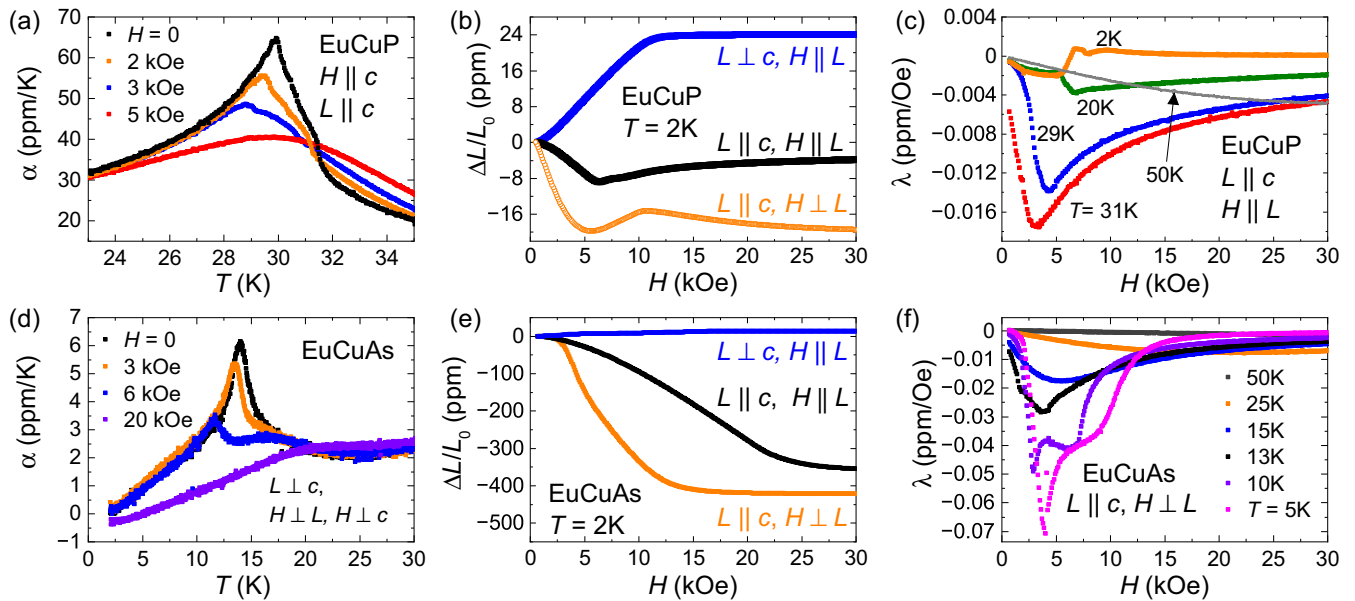
FIG. 7. Dilatometry data for EuCuP [upper panels, (a)–(c)] and EuCuAs [lower panels, (d)–(f)] in various applied fields. (a), (d) Thermal expansion coefficients near the magnetic transitions under different applied fields with orientations provided. (b), (e) Field dependence of the dilation at $T = 2$ K with different orientations of applied field and dilation. (c), (f) Magnetostriction coefficients at select temperatures with fields applied along the easy axis of EuCuP and easy plane of EuCuAs.

The field-dependent dilation and isothermal magnetostriction (field derivative of the dilation) of EuCuP are shown in Figs. 7(b) and 7(c). These data reveal a complex evolution of the lattice with applied field. The field-dependent dilation is expected to be related to the size of the induced moment (or the susceptibility), and thus the dilatometry data suggest a complex evolution of the magnetization as the moment approaches saturation for fields applied along the [001] easy axis. Specifically, multiple features can be observed in Fig. 7(c) near the saturation field at $T = 2$ K, and small kinks in the data are observed at higher temperatures. These data therefore complement thermal expansion data at low fields, which suggest multiple magnetic phases may be present in EuCuP, though the potential role of domains is unclear. In total, these results suggest that there are two phase transitions near T_C in EuCuP and that the system may host a noncollinear magnetic structure such as a helix. Detailed neutron diffraction studies should be performed to investigate this behavior, although care must be taken due to absorption caused by Eu. Resonant x-ray scattering also offers a viable means to track this behavior, as demonstrated by investigations of the incommensurate magnetism in isostructural EuZnGe [67].

The thermal expansion behavior of EuCuAs around T_N was shown in Fig. 6(c) and the impact of applied fields is examined in Fig. 7(d). The data presented focus on dilation with $H \perp c$ because this is the orientation where the metamagnetic transition occurs and is thus the crystallographic plane where the moments are primarily oriented in zero field. Consistent with antiferromagnetic character, the application of a magnetic field suppresses the peak in the thermal expansion coefficient that occurs near T_N. As the applied field increases, though, it is interesting to see a well-defined but broad bump in α above T_N, which eventually dominates at the highest fields where the moments are polarized at low T (and a small

region of negative thermal expansion is observed). Isothermal measurements as a function of field are shown for EuCuAs in Figs. 7(d) and 7(f) and the magnetostriction coefficient data emphasize expansion along [001], which is the direction where the largest response to the magnetic ordering was observed. The magnetostriction increases continually upon cooling as seen in Fig. 7(f). In this orientation, the thermal expansion coefficient at $H = 0$ peaks above T_N near 15 K [see Fig. 6(c)]. In terms of the magnetostriction, the behavior at 15 K has similar field dependence to the data at 13 K but the higher temperature data lack the sharp features seen below T_N. Upon cooling further, these features evolve into a sharp and distinct minimum at the metamagnetic transition (near 4 kOe at 5 K) and there is a broader feature at slightly higher fields that occurs on the way to saturation as the magnetostriction coefficient goes toward zero. As some lattice responses to the metamagnetic transition are expected and observed, the data help validate the use of similar results for EuCuP being taken as evidence of possible field-induced transitions, which in turn imply that the zero-field state is not simply ferromagnetic, though domain effects may play a complicating role.

The field-dependent dilation data presented in Figs. 7(b) and 7(e) reveal interesting similarities between EuCuP and antiferromagnetic EuCuAs. The lattices expand within the basal plane and contract along the [001] orientation when the moments are polarized, regardless of the orientation of the applied field. Quantitatively, however, a much larger field-induced change in the lattice occurs for EuCuAs than in EuCuP, especially for dilation along [001]. However, in zero field, the relative change in dilation is larger for EuCuP than for EuCuAs (a larger initial $H = 0$ contraction of the lattice).

These results suggest that the dominant characteristic determining the size of magnetoelastic coupling in these
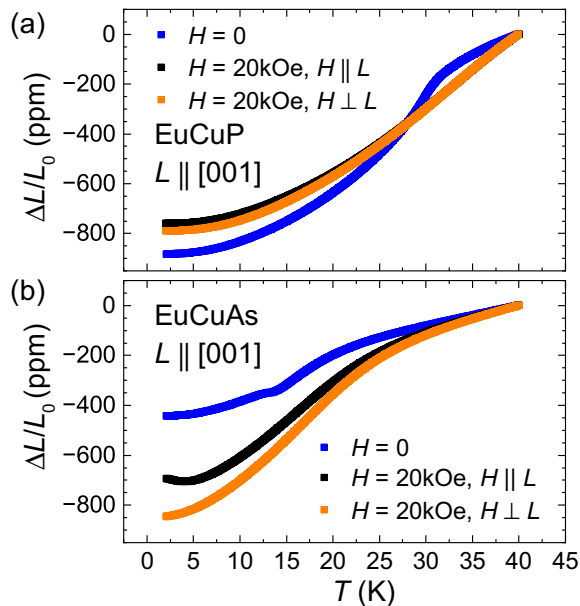
FIG. 8. Relative dilation along [001] in zero field and $H = 20$ kOe applied both parallel and perpendicular to [001] for (a) Eu-CuP and (b) EuCuAs. Data were collected upon cooling and made relative the sample length at 40 K. Lattice changes are found to be relatively independent of the direction of the field (moments), indicating that it is the spin coupling and not the magnetic anisotropy that dominates the magnetoelastic effects in this family. A small region of negative thermal expansion is observed for EuCuAs when the field is parallel to the dilation along [001].

materials is the sign of the largest magnetic exchange interaction and not the anisotropy or orientation of the moments. This hypothesis is further supported by considering the temperature-dependent dilation with an applied field of 20 kOe, which is above the saturation field for both EuCuP and EuCuAs regardless of orientation. These data are shown in Fig. 8 for dilation along [001] and the field is applied along [001] or [100]. In EuCuP, the applied field does not have a significant impact on the net dilation observed, while in EuCuAs there is indeed a large lattice response to the applied field. Furthermore, the orientation of the applied field does not have a significant impact. Therefore, the orientation of the moments (magnetic anisotropy) does not have a large impact on the net dilation, but the coupling of the moments does. Specifically, the dominant antiferromagnetic coupling in EuCuAs appears to suppress the net dilation, implying that the ferromagnetic coupling of spins leads to stronger magnetoelastic coupling in these materials regardless of orientation of the spins. This is also supported by the observation that the dilation of EuCuAs approaches that of EuCuP when a large field is applied. These results also reveal that the applied field impacts the expansion behavior well above the ordering transition in both systems, as may be expected for the large moment systems where the energy of the applied field is amplified or perhaps is evidence of strong correlations in the paramagnetic state. These results have implications for spin-polarized first-principles calculations that attempt to understand electronic topology; the impact of lattice relaxations must be taken into consider-

ation. Due to the different ordering temperatures, it might not make sense to make detailed comparisons above the ordering transitions because the data were made relative to dilation at $T = 40$ K to allow for a direct comparison. However, it appears that the applied field has a larger impact at high T in EuCuAs. It is thus worth recalling that EuCuAs also has a positive Weiss temperature and indications of some ferromagnetic order are inferred from the out-of-phase contribution to the ac susceptibility possessing a peak above T_N in EuCuAs. Thus, in reconsidering the anisotropy of the thermal expansion coefficient of EuCuAs, the peak in α along [001] above T_N may be related to short-range ferromagnetic correlations that are overcome by dominant antiferromagnetic coupling.

Using the total specific heat and anisotropic thermal expansion data, the Gruneisen ratios $\gamma = \alpha/C_P$ were computed for EuCuP and EuCuAs and the data are included in Fig. 13 in the Appendix. The qualitative behavior of γ generally tracks that of α, with the notable exception that γ of EuCuP remains large upon cooling to base temperature while that of EuCuAs goes toward zero. The anisotropy is also highlighted, with the feature at 30 K dominant for [001] and the feature at 31.25 K dominant for the [100] orientation in EuCuP. Similarly, the peak in EuCuAs for the [100] orientation appears amplified while for the [001] orientation the broad maximum occurs above T_N and a sharp minimum occurs below T_N. Due to the large α along [001] the γ values in this orientation are larger than those in the basal plane. These are the total Gruneisen ratios, combining effects of both magnetism and the lattice contributions.

E. Thermal transport

Thermal conductivity κ provides a complementary probe of the interaction between the lattice dynamics and the magnetism. While magnons can carry heat and lead to enhanced κ in a magnetically ordered phase, magnons can scatter phonons and suppress κ. In addition, spin fluctuations or short-range order that couples to the lattice may also scatter phonons in the paramagnetic state.

The in-plane thermal conductivity data are shown in Fig. 9, and these data reveal a strong impact of the magnetic transition on the lattice thermal conductivity in EuCuP but not in EuCuAs. Through simple analysis, the thermal conductivity is found to be dominated by the lattice contribution κ_L. The lack of a clear anomaly in EuCuAs appears to be additional evidence of a smaller spin-phonon coupling effect in EuCuAs as compared to EuCuP where a clear impact on κ is observed in both the electronic and lattice contributions. The location of the magnetic ordering temperature relative to the maximum in κ_L may also play a role, as the peak in κ_L is generally related to the relative importance of the temperature dependence of the lattice's heat capacity and the various phonon scattering mechanisms that limit the phonon mean-free paths, and these competing contributions could impact the ability to see the effect of a changing spin-phonon scattering rate in EuCuAs. The lattice thermal conductivity κ_L was estimated using the Wiedemann-Franz law to subtract the electronic contribution $\kappa_e = L_0\sigma T$ where $\sigma = 1/\rho$ and the ρ data are shown in Fig. 11(a). To accomplish this, fully degenerate Fermi statistics were assumed for the Lorenz number L_0 [68],
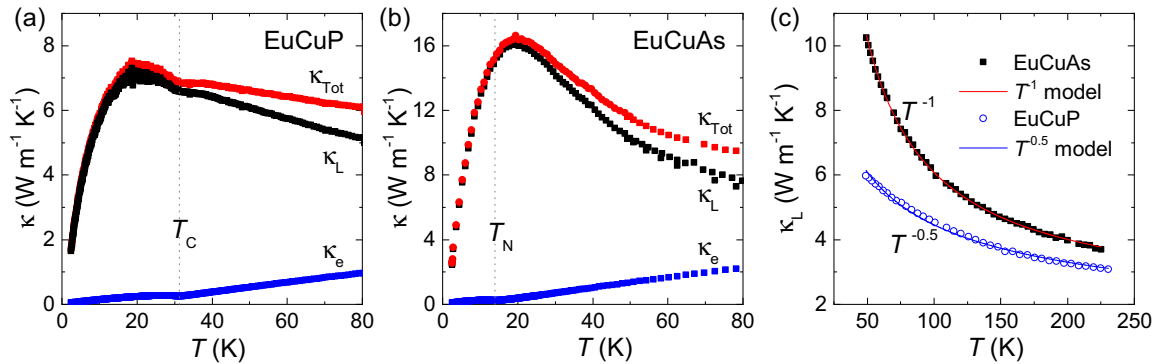
FIG. 9. (a), (b) Measured in-plane thermal conductivity κ_{Tot} of (a) EuCuP and (b) EuCuAs with electronic κ_e and lattice κ_L contributions estimated as described in the text. (c) Estimated lattice contributions at high temperatures demonstrating the reduced temperature dependence in EuCuP that is believed to be linked to spin-phonon scattering at high temperatures. The qualitative $\kappa_L = \kappa_0 + A/T^p$ model is described in the text.

which seems reasonable based upon the small value of the Seebeck coefficient that was measured (see below).

The scattering by magnetic fluctuations well above T_C likely leads to the suppressed κ_L of EuCuP relative to that of EuCuAs in the paramagnetic regimes [Fig. 9(c)]. In turn, this leads to a slower decay with increasing temperature. Specifically, the T^{-1} decay of κ_L observed in EuCuAs above 50 K is typical for that of a crystalline system where phonon-phonon scattering dominates. The existence of additional scattering mechanisms with different temperature dependencies can lead to a deviation from this, and indeed for EuCuP the decay is closer to $T^{-0.5}$ as illustrated in Fig. 9(c). In Fig. 9(c), a simple $\kappa_L = \kappa_0 + A/T^p$ was utilized to qualitatively model the temperature dependence of κ_L. The term κ_0 represents a high-temperature minimum or other temperature-independent contributions, and the exponent p was fixed at either 0.5 or 1 after least-squares fitting resulted in similar values.

For typical crystalline lattices, one might expect the thermal conductivity of EuCuP to be greater than that of EuCuAs because of the higher Debye temperature (thus higher acoustic phonon velocities) in EuCuP due to the lower average atomic mass. Of course, the optical phonons may play a significant role in these systems too, so one must be careful with simplifications. However, it is interesting to point out that the Gruneisen ratios were much larger in EuCuP than in EuCuAs, and this would generically point to higher anharmonicity in the phosphide. Such results may prove useful when considering the thermoelectric properties of related phases.

F. Mössbauer spectroscopy

Due to the observation of closely spaced features near the Curie temperature in the physical properties, Mössbauer spectroscopy was performed to investigate the possibility of an evolving magnetic structure in EuCuP. The results are summarized in Fig. 10.

The spectra at $T = 36$ K and higher exhibit a sharp single component with isomer shift, $\delta = -10.5(1)$ mm/s, which is characteristic of Eu^{2+} [35]. At room temperature, we find that at most 1% of the spectral area can be attributed to Eu^{3+} with $\delta = 0.8(3)$ mm/s. Onset of magnetic hyperfine splitting (strong magnetic correlations and magnetic ordering)

is observed at 34 K and the hyperfine field reaches $\mu_0 H_{hf} = 29.1(1)$ T at $T = 8.5$ K, as shown in Fig. 10(b). The magnetic spectra exhibit a small asymmetry indicative of the presence of a quadrupole splitting ΔE_Q. Referring to the paramagnetic spectra we determined that ΔE_Q is ≈ -3 mm/s, which we used for a starting point for fits of the magnetic spectra.

In order to fit the spectra, we used a single spectral component for Eu^{2+} and a small Eu^{3+} impurity component that stayed constant in area and isomer shift for all temperatures. The crystal symmetry dictates an axial electric field gradient (EFG) with null asymmetry $\eta = 0$. This leaves five fit parameters: δ, ΔE_Q, H_{hf}, θ, Γ, with θ the angle between the EFG principal axis and the hyperfine field and Γ the line full width at half-maximum. For all temperatures, $\delta = -10.5(2)$ mm/s, with no noticeable second-order Doppler shift; lines are rather narrow, $\Gamma = 2.4(2)$ mm/s, below 34 K and broaden significantly at the paramagnetic transition $\Gamma = 3.8(5)$ mm/s, due to saturation, before narrowing down to $\Gamma = 2.4(2)$ mm/s at 295 K. There is a correlation between ΔE_Q and θ and fitting both parameters does not significantly improve the fits; fixing ΔE_Q to its value in the paramagnetic phase leads to $\theta = 8(5)$ degrees. Hence, we fitted all spectra with $\theta = 0$, and found a stable and constant value of $\Delta E_Q = -2.5(5)$ mm/s for all magnetic spectra.

The temperature dependence of the hyperfine field is reported in Fig. 10(b). At 34 K, the spectrum exhibits 35% of paramagnetic fraction; the reported hyperfine field is that of the ordered fraction. Because there is indication of a coupling of the magnetic order with the thermal expansion, we have utilized a magnetostriction exchange model [69] to fit the temperature dependence of the europium hyperfine field [see Fig. 10(b)]. This magnetostriction model represents the data significantly better than a simple mean-field model, and the magnetostriction parameter fitted to the data is $\eta = 0.33$, i.e., $0 < \eta < 1$ in the second-order transition range [69].

The observed spectra indicate that europium exhibits a static moment in the ordered state and a single Eu^{2+} valence state, as indicated previously in Ref. [48]. In addition, the spectra demonstrate that the moment is not modulated in magnitude, and thus a spin density wave does not appear to exist in EuCuP (even close to T_C as demonstrated by the
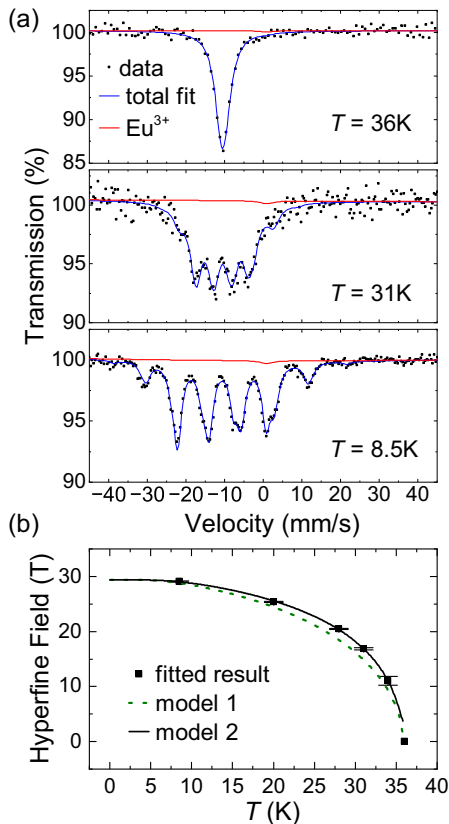
FIG. 10. (a) ^{151}Eu Mössbauer spectra of EuCuP at the indicated temperatures above and below the Curie temperature near 31.25 K. The total fit and that of the Eu^{2+} contribution is nearly indistinguishable, so only the total fit (blue) and the Eu^{3+} contribution (red) are shown in comparison to the data (black markers). (b) Temperature dependence of the Eu^{2+} hyperfine field in EuCuP obtained from Mössbauer spectroscopy. The (green dotted) and (black) lines are guides for the eye representing mean-field behavior for a spin $\frac{7}{2}$ with $T_C = 35$ K with (model 2) and without (model 1) exchange magnetostriction, respectively.

data collected at 31 K in the vicinity of the complex phase transition evidenced by dilatometry and specific heat). For comparison, spectra associated with amplitude-modulated Eu moments were reported for orthorhombic EuPdSb, where a distribution of hyperfine fields (moment amplitudes) causes a general broadening of spectral features [70]. It is possible that the temperature steps we utilized for measurements of EuCuP precluded detection of such a phase in a small temperature range near the Curie temperature. Regardless, a modulation in the *direction* of the moment (commensurate or incommensurate) cannot be ruled out from the data at hand. This is due to the local nature of Mössbauer spectroscopy and the fact that each Eu ion would experience a similar hyperfine field even if the orientation of that field is changing.

Within the family of related compounds [35], the isomer shift for EuCuP is at the more negative end. A value of $\delta = -10.8$ mm/s was reported earlier at room temperature [48]. However, as expected, considering that EuCuP has the smallest unit-cell volume in the EuMPn family it has also the largest isomer shift [35,63] in the family; to conclude this

we used the observed volume dependence in high pressure on elemental Eu that indicates an increase in isomer shift with decreasing volume [71]. The hyperfine field is on par with the 29.6 T in EuPtSb [63], which is the largest reported value in this family of ternary Eu-containing compounds; the hyperfine field in EuCuP is also the largest observed in the EuMPn family and this correlates with the largest Weiss temperature [37] and highest ordering temperature.

G. Electronic transport

EuCuP and EuCuAs both possess metallic conductivity with a sharp peak in the resistivity near their magnetic ordering temperatures [49,50,52], as illustrated in Fig. 11(a). Well above the ordering temperatures, in their paramagnetic states, the resistivity of these crystals increases nearly linearly with increasing T. The temperature dependence is similar to that observed for nonmagnetic CaCuAs. This is typical for degenerate (metallic) materials when electronic relaxation times are limited by phonon scattering [68].

The resistivity values for EuCuP and EuCuAs are much larger than those of CaCuAs. This is primarily an effect of carrier mobility, not carrier densities, as shown in Fig. 11(b). The carrier mobility is impacted by the relaxation time and the carrier's effective mass. The magnetism in EuCuP and EuCuAs appears to significantly suppresses the carrier mobility, likely through a reduction of carrier lifetime though the presence of Eu may act to modify the effective mass of the valence band in these materials. Recent calculations have shown negligible amount of Eu $4f$ states near the Fermi surface [50]. Our data also reveal a higher mobility in EuCuAs than in EuCuP, though they are similar in magnitude and the mobility varies between samples as the carrier density changes (see Fig. 14 in the Appendix).

For EuCuP, we observed a rather large distribution of Hall carrier densities ($\approx 3 \times 10^{20}$ to 3×10^{21} cm^3) between different crystals, even when comparing across a single-crystal growth batch. A summary plot is shown in Fig. 14 in the Appendix, where the ac susceptibility is also shown for the different crystals. These results show that the qualitative features are consistent between different crystals, but that different defect concentrations (doping levels) impact how dramatic the peak at the magnetic ordering transition appears to be. In addition, the observed differences in ac susceptibility are likely further complicated by changes in the demagnetization effects due to sample geometry, even for these low-field measurements, as also illustrated in Fig. 12 the Appendix.

For the samples shown in Fig. 11, the Hall densities obtained at $T = 100$ K are as follows: EuCuP, 8.3×10^{20} cm^{-3}; EuCuAs, 5.8×10^{20} cm^{-3}; and CaCuAs, 6.2×10^{20} cm^{-3}. These hole concentrations were computed assuming a single parabolic band, with Hall coefficients obtained from a fit to the field dependence of the odd-only transverse resistance that was linear with field, all data above $H = 20$ kOe being fit; representative Hall resistance data for the crystals in Fig. 11 are shown in the Appendix Fig. 15. The magnetic field is applied along the c axis in the Hall effect measurements.

Iha *et al.* reported an apparent increase in the Hall density across the magnetic transition in EuCuP [49], though not
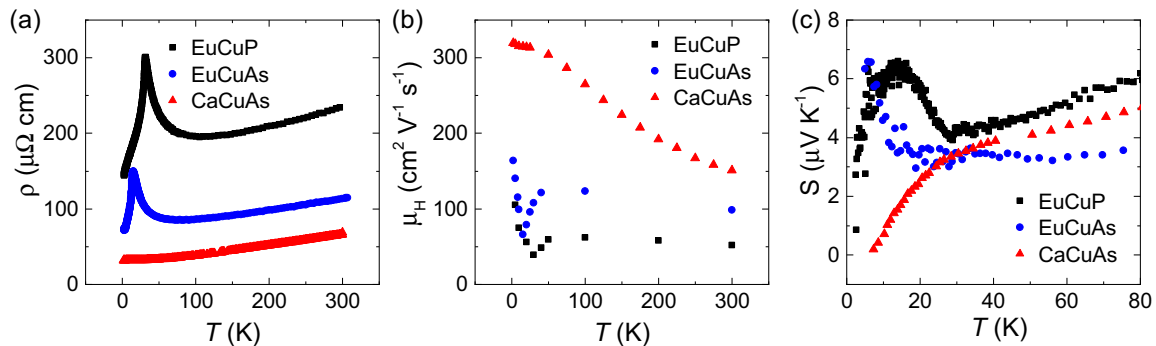
FIG. 11. (a) In-plane electrical resistivity and (b) Hall mobility for EuCuP, EuCuAs, and nonmagnetic CaCuAs. (c) Seebeck coefficients revealing an increasing component upon cooling below T_C (T_N) in EuCuP (EuCuAs) and nonlinearity in $S(T)$ for CaCuAs. The mobility was obtained from resistivity and Hall measurements on different crystals than that utilized in (a) and (c) due to geometric requirements for the Seebeck effect for EuCuAs and EuCuP; see Fig. 14 in the Appendix for property distribution across different EuCuP crystals and Fig. 15 for representative data of the Hall resistances versus magnetic field.

much variation is observed above the ordering temperatures. We observed a similar effect in both EuCuP and EuCuAs, for all crystals, but it is not clear if this is due to inclusion of an anomalous (magnetic) contribution. Similar nonlinear field dependence was observed in EuB$_6$ [53,55], however, and thus there may be connections to the magnetic polarons reported in that material. The Hall voltage of CaCuAs was very linear across all magnetic fields at all temperatures explored. Efforts are underway to understand this complex behavior in greater detail, and a recent study of the magnetotransport on EuCuP was performed by Wang *et al.* [50], where the anomalous Hall contribution is discussed in detail. The qualitatively similar field dependence of the Hall resistance in EuCuP and EuCuAs is interesting given the different types of magnetic order in these materials.

Seebeck effect measurements were performed to better understand the electronic structure in these materials. The Seebeck coefficients S were found to be small and positive, indicating p-type conduction with metallic behavior. This is consistent with the Hall effect, which produced a positive Hall coefficient (hole doped). Taken together, these results suggest that the EuCuP and EuCuAs crystals grown from a Sn flux contain intrinsic defects that remove electrons from the valence band and result in nearly degenerate carrier conduction. The contribution of a small concentration of electrons (n type) may go unnoticed in these measurements. In this formalism, the resistivity is expected to increase with increasing temperature until carrier activation across the gap (or within the semimetal state) causes the resistivity to peak and start decreasing as intrinsically excited carriers begin to dominate conduction. Resistivity measurements on a EuCuP crystal to approximately 600 K did not observe the effects of carrier activation, presumably due to the relatively large number of free carriers introduced by apparent defects ("extrinsic" carriers in the sense of semiconductor physics, though in this case they are caused by "intrinsic" defects).

The Seebeck coefficients of EuCuP and EuCuAs begin to increase upon cooling into the magnetically ordered states. There does not appear to be any clear effect above the ordering transitions, making this behavior different from the resistivity

(mobility) where a large change occurs upon cooling towards T_C (T_N) for EuCuP (EuCuAs). Instead, there is a small dip in S right near T_C for EuCuP and then a couple degrees lower S starts to increase. This behavior made us consider some type of magnon drag effect, though the qualitative temperature dependence did not seem to fit and the effect was enhanced with an applied field. For normal scattering effects, the Seebeck coefficient is not impacted by the electron's relaxation time, but instead is impacted by the energy dependence of the relaxation time (this is usually not an observed effect, simply part of the modeling within Boltzmann transport theory). In considering this, it thus seemed likely that the enhanced Seebeck coefficient originates from phonon drag, which is a well-established effect at low T in conducting materials ranging from metals to semiconductors. The decreased hole-spin or phonon-spin interactions likely enable the drag effect to occur. To probe this further, we measured the Seebeck coefficient of a small CaCuAs crystal using a home-built apparatus. Above ≈ 40 K, the temperature dependence of S is rather similar in CaCuAs and EuCuP. However, in a degenerate conductor like this, one would expect S to tend toward zero in a linear manner. The fact that the high-T portion extrapolates to a nonzero value suggests that some additional contribution is at play, such as phonon drag or complexity in the electronic structure (transition between number of bands contributing to conduction). The phonon-drag conjecture would admittedly be more convincing if there was a peak in S for CaCuAs, and thus more consideration may be necessary. The upturn in S for EuCuP occurs at a slightly higher temperature when a magnetic field is applied parallel to the thermal flux, and the peak value is similar; this is assumed to be driven by changes in the carrier mean-free path caused by the magnetic field (i.e., effects of the magnetoresistance).

IV. SUMMARY

The magnetoelastic coupling and phase transitions in EuCuP and EuCuAs were examined through dilatometry, thermal and thermoelectric transport, specific-heat capacity, and magnetization measurements on single crystals grown in a

Sn flux. EuCuP was found to have a larger magnetoelastic coupling than EuCuAs at zero field. The impact of an applied field on the lattice was larger for EuCuAs than for EuCuP. These observations suggest that the dominant ferromagnetic coupling of spins in EuCuP leads to a larger zero-field magnetoelastic coupling as compared to that in antiferromagnetic EuCuAs. It may be challenging to separate the magnetic and lattice contributions to the Grüneisen ratios (Fig. 13) in these types of materials.

The magnetic ordering transition in EuCuP appears to occur through two steps, with features near 31.25 and 30 K in dilation and specific-heat measurements. Furthermore, these anomalies are slightly suppressed by applied fields, making the ferromagnetic picture appear less appropriate. Mössbauer spectroscopy measurements were performed in an attempt to uncover an evolving magnetic structure, but these measurements did not reveal an amplitude-modulated phase and a continuous evolution of the hyperfine field with T was observed; a modulation of the moment orientation is not ruled out. Neutron diffraction or similar measurements appear necessary to probe the nature of the magnetic phases in EuCuP, with care taken to look for unique phases near the Curie temperature. For EuCuAs, ac susceptibility measurements revealed impacts of short-range order above T_N that appear to be ferromagnetic in nature, and these may drive the complex evolution of the lattice expansion near the antiferromagnetic transition.

The EuCuP and EuCuAs crystals grown from a Sn flux have similar electrical properties, with Hall carrier numbers in the range of 10^{20}–10^{21} cm^{-3}. This implies some intrinsic defects, likely Eu or Cu vacancies, and controlling these defects would be critical to future measurements aimed at understanding any potential electronic topology in these materials. In our EuCuP/EuCuAs crystals, p-type behavior was prevalent with similar apparent doping and defect concentrations between the different materials, though variation within a growth batch exists. Controlling defects in narrow-gap semiconductors or semimetals is a major challenge in materials physics. Crystal growth conditions often dictate the types and concentrations of defects, though in some materials certain defects are likely to be energetically favorable and present regardless of the synthesis techniques utilized. It is generally accepted to be very challenging to form electron-doped (n-type) Zintl pnictides. For instance, in the AZn$_2$Sb$_2$ (A=Ca,Yb,Eu) Zintl compounds, vacancies of the divalent A-site cations are thermodynamically stable under common synthesis conditions but should also form as compensating defects when the Fermi level rises [72]. Since the behavior is driven by thermodynamics, it may be possible to manipulate the concentrations of defects by changing the thermodynamic environment during the growth. This has been demonstrated in EuCd$_2$Sb$_2$, where growth in a Sn flux leads to antiferromagnetic behavior but controlled growth in a salt flux can produce ferromagnetic behavior, with trends linked to changes in the Fermi energy associated with varying concentrations of Eu vacancies [20]. With regards to EuMPn materials, vacancies of the monovalent cation Cu/Ag are reported to be stable in CaCuP and CaAgP [73,74]. Obtaining semiconducting behavior in narrow-gap systems remains a great challenge. As such, dedicated synthesis efforts could play a pivotal role in this area of materials physics, with theoretical calculations likely providing very valuable input. The contraction of the lattice due to magnetic ordering may also impact the electronic structures and would be good to consider during first-principles calculations that are aimed at understanding the fine details and topology of the electronic structure.

APPENDIX

This Section includes a graphical overview in Fig. 12 of the impact that the geometric demagnetization factor has on the measured magnetization when the data are plotted versus the applied field H. A schematic is shown to illustrate how the sample geometry changes (via mechanical polishing) from a cube to a thin plate, with the area perpendicular to the magnetic field being reduced as the sample is polished. By reducing this area while leaving the other dimensions of the cube unchanged, the geometric demagnetization factor is reduced and thus the demagnetizing field is also reduced. Further details are provided in the caption.

Additional plots that complement the main text are also provided for the interested reader. The Gruneisen ratios are plotted in Fig. 13 and these contain both the lattice and magnetic portions. Figure 14 contains data for various EuCuP single crystals to demonstrate the differences observed between different crystals. Finally, Fig. 15 contains the antisymmetrized Hall resistivity as a function of applied field. The datasets are for the crystals corresponding to the data in Fig. 11(b). Further details are given in each caption.
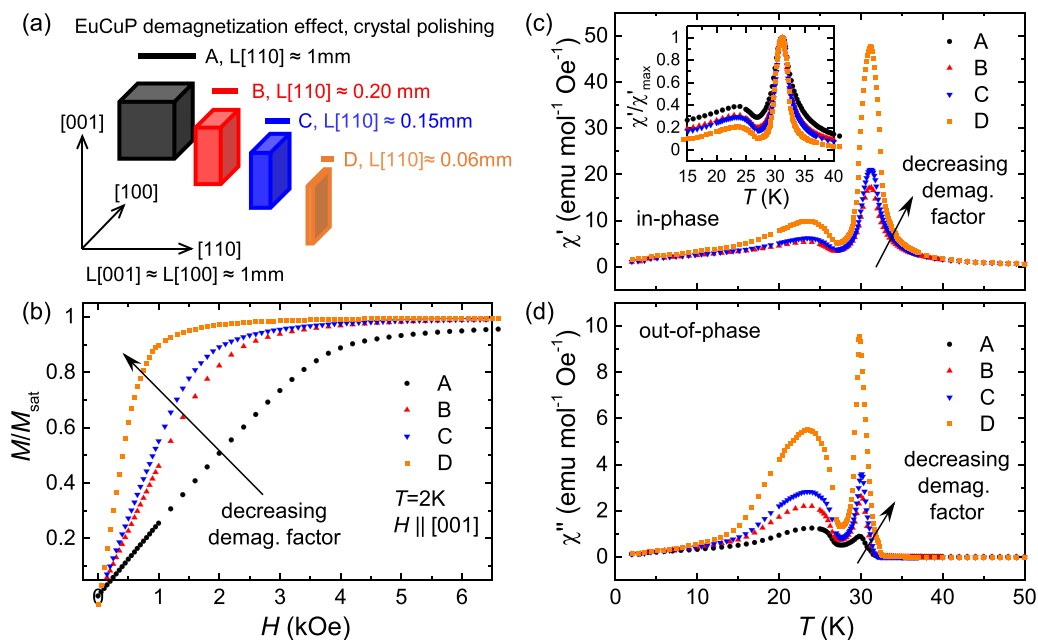

FIG. 12. Impact of geometric demagnetization factor on magnetization data with $H \parallel c$ for EuCuP. The geometric demagnetization factor (and thus demagnetization field) is physically reduced upon going from stage A to D, and thus the data for stage D are expected to be closest to the intrinsic results. (a) Schematic of the sample polishing and measurement stages starting with an approximate cube in stage A, which was subsequently polished along [110] to reduce the surface area perpendicular to the applied field. (b) Isothermal magnetization data at $T = 2$ K showing the expected shift as the importance of the demagnetization effect is reduced. This leads to an increase in the measured susceptibility [slope of $M(H)$]. (c) Change of in-phase and (d) out-of-phase contributions to the ac susceptibility as the demagnetization factor is modified. A large demagnetization field results in an effective suppression of the peak in χ that occurs near the Curie temperature. The peak itself is impacted more than other parts of this curve, and thus geometric effects can artificially enhance the relative importance of additional features, such as the anomaly near 25 K (see inset for normalized χ'/χ'_{max}). Data in Figs. 3(a) and 3(c) and 4(a) and 4(b) of the main text were collected at stage B of this process.
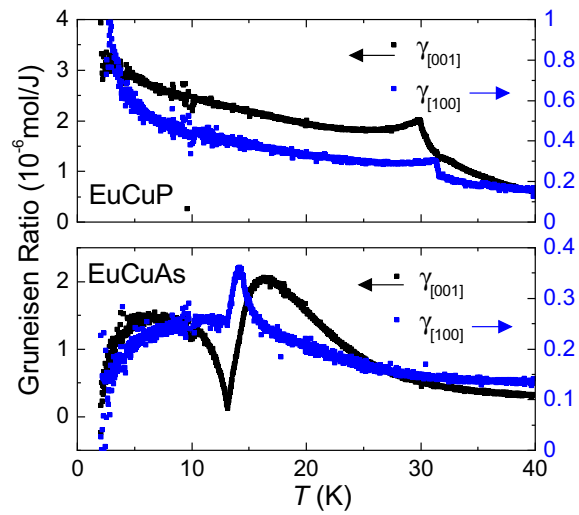
FIG. 13. Anisotropic Gruneisen ratios for EuCuP (upper panel) and EuCuAs (lower panel) obtained from the thermal expansion and specific-heat data as $\gamma = \alpha/C_P$. The left and right axes share the same units, with the smaller values of γ on the right axis associated with the in-plane expansion data.
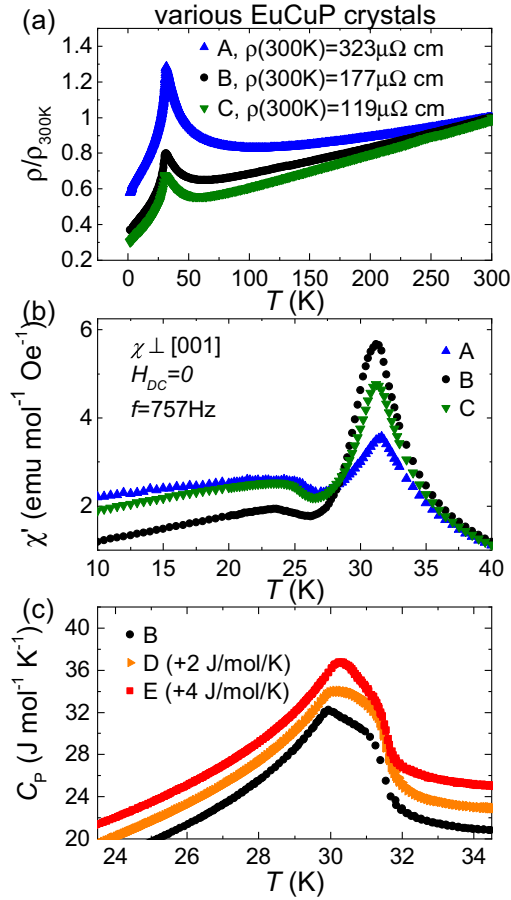
FIG. 14. Comparison of (a) electrical resistivity, (b) ac susceptibility, (c) specific-heat capacity for different EuCuP crystals; crystals A,B,C are from one growth while D,E are from another growth. (a) The resistivity ratio is shown versus temperature and (b) the in-phase contribution to the ac susceptibility. The more metallic crystals with lower absolute resistivity have a smaller change in resistivity near the magnetic transition. The difference in absolute resistivity was tracked with a change in p-type Hall carrier density, with values for different crystals obtained at 50 K from the linear high-field Hall data as follows: A, 3.1×10^{20} cm^{-3}; B, 9.0×10^{20} cm^{-3}; C, 2.5×10^{21} cm^{-3}. Crystals with higher carrier densities also have a lower carrier mobility (37–66 cm^2/V/s at 50 K), consistent with additional scattering from a higher concentration of defects as well as the general expectation of increased electron-phonon scattering with increasing carrier density in degenerate semiconductors [68]. The resistivity peak occurs at slightly different temperatures and small changes in the ac susceptibility are also observed, though the impacts of demagnetization effects are expected to be large due to widely varying sample geometries in these different crystals.
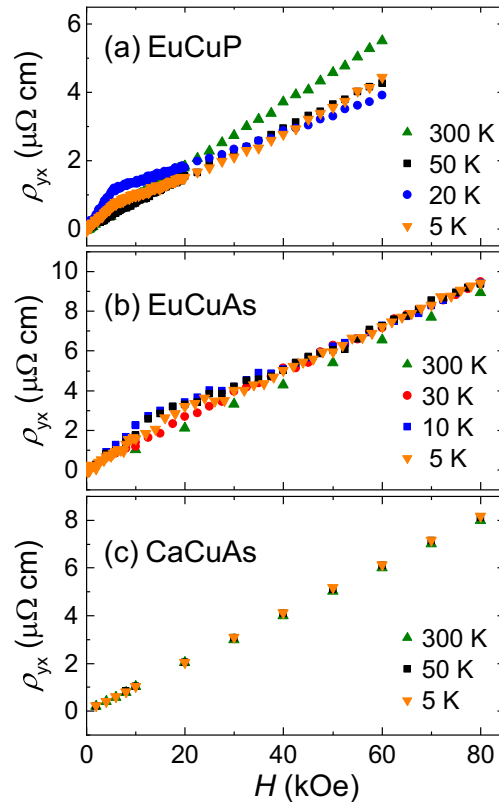
FIG. 15. Representative Hall resistance (antisymmetrized) versus magnetic field at select temperatures for (a) EuCuP, (b) EuCuAs, and (c) CaCuAs. The data were collected on the crystals utilized to compute the Hall mobility data in Fig. 11(b), for which linear fits above 20 kOe were utilized to obtain the Hall coefficients.

[1] J.-Q. Yan, Q. Zhang, T. Heitmann, Z. Huang, K. Y. Chen, J.-G. Cheng, W. Wu, D. Vaknin, B. C. Sales, and R. J. McQueeney, Crystal growth and magnetic structure of $MnBi_2Te_4$, Phys. Rev. Mater. **3**, 064202 (2019).

[2] S. H. Lee, Y. Zhu, Y. Wang, L. Miao, T. Pillsbury, H. Yi, S. Kempinger, J. Hu, C. A. Heikes, P. Quarterman, W. Ratcliff, J. A. Borchers, H. Zhang, X. Ke, D. Graf, N. Alem, C. Z. Chang, N. Samarth, and Z. Mao, Spin scattering and noncollinear spin structure-induced intrinsic anomalous hall effect in antiferromagnetic topological insulator $MnBi_2Te_4$, Phys. Rev. Res. **1**, 012011(R) (2019).

[3] D. Zhang, M. Shi, T. Zhu, D. Xing, H. Zhang, and J. Wang, Topological Axion States in the Magnetic Insulator $MnBi_2Te_4$ With the Quantized Magnetoelectric Effect, Phys. Rev. Lett. **122**, 206401 (2019).

[4] M. M. Otrokov, I. P. Rusinov, M. Blanco-Rey, M. Hoffmann, A. Y. Vyazovskaya, S. V. Eremeev, A. Ernst, P. M. Echenique, A. Arnau, and E. V. Chulkov, Unique Thickness-Dependent Properties of the Van Der Waals Interlayer Antiferromagnet $MnBi_2Te_4$ Films, Phys. Rev. Lett. **122**, 107202 (2019).

[5] J. Li, Y. Li, S. Du, Z. Wang, B.-L. Gu, S.-C. Zhang, K. He, W. Duan, and Y. Xu, Intrinsic magnetic topological insulators in van der waals layered $MnBi_2Te_4$-family materials, Sci. Adv. **5**, eaaw5685 (2019).

[6] K. He, $MnBi_2Te_4$-family intrinsic magnetic topological materials, npj Quantum Mater. **5**, 90 (2020).

[7] M. M. Otrokov, I. I. Klimovskikh, H. Bentmann, D. Estyunin, A. Zeugner, Z. S. Aliev, S. Gaß, A. Wolter, A. Koroleva, A. M. Shikin *et al.*, Prediction and observation of an antiferromagnetic topological insulator, Nature (London) **576**, 416 (2019).

[8] L. Jiao, Q. Xu, Y. Cheon, Y. Sun, C. Felser, E. Liu, and S. Wirth, Signatures for half-metallicity and nontrivial surface states in the kagome lattice weyl semimetal $Co_3Sn_2S_2$, Phys. Rev. B **99**, 245158 (2019).

[9] N. Morali, R. Batabyal, P. K. Nag, E. Liu, Q. Xu, Y. Sun, B. Yan, C. Felser, N. Avraham, and H. Beidenkopf, Fermi-arc diversity on surface terminations of the magnetic weyl semimetal $Co_3Sn_2S_2$, Science **365**, 1286 (2019).

[10] D. Liu, A. Liang, E. Liu, Q. Xu, Y. Li, C. Chen, D. Pei, W. Shi, S. Mo, P. Dudin *et al.*, Magnetic weyl semimetal phase in a kagomé crystal, Science **365**, 1282 (2019).

[11] A. Rossi, V. Ivanov, S. Sreedhar, A. L. Gross, Z. Shen, E. Rotenberg, A. Bostwick, C. Jozwiak, V. Taufour, S. Y. Savrasov, and I. M. Vishik, Electronic structure and topology across T_c in the magnetic weyl semimetal $Co_3Sn_2S_2$, Phys. Rev. B **104**, 155115 (2021).

[12] A. M. Goforth, P. Klavins, J. C. Fettinger, and S. M. Kauzlarich, Magnetic properties and negative colossal magnetoresistance of

the rare earth zintl phase $EuIn_2As_2$, Inorg. Chem. **47**, 11048 (2008).

[13] Y. Xu, Z. Song, Z. Wang, H. Weng, and X. Dai, Higher-Order Topology of the Axion Insulator euin$_2$as$_2$, Phys. Rev. Lett. **122**, 256402 (2019).

[14] Y. Zhang, K. Deng, X. Zhang, M. Wang, Y. Wang, C. Liu, J.-W. Mei, S. Kumar, E. F. Schwier, K. Shimada, C. Chen, and B. Shen, In-plane antiferromagnetic moments and magnetic polaron in the axion topological insulator candidate $EuIn_2As_2$, Phys. Rev. B **101**, 205126 (2020).

[15] S. X. Riberolles, T. V. Trevisan, B. Kuthanazhi, T. Heitmann, F. Ye, D. Johnston, S. Bud'ko, D. Ryan, P. Canfield, A. Kreyssig *et al.*, Magnetic crystalline-symmetry-protected axion electrodynamics and field-tunable unpinned dirac cones in $EuIn_2As_2$, Nat. Commun. **12**, 999 (2021).

[16] J. Yan, Z. Z. Jiang, R. C. Xiao, W. J. Lu, W. H. Song, X. B. Zhu, X. Luo, Y. P. Sun, and M. Yamashita, Field-induced topological hall effect in antiferromagnetic axion insulator candidate $EuIn_2As_2$, Phys. Rev. Res. **4**, 013163 (2022).

[17] M. Gong, D. Sar, J. Friedman, D. Kaczorowski, S. Abdel Razek, W.-C. Lee, and P. Aynajian, Surface state evolution induced by magnetic order in axion insulator candidate $EuIn_2As_2$, Phys. Rev. B **106**, 125156 (2022).

[18] J.-R. Soh, F. de Juan, M. G. Vergniory, N. B. M. Schröter, M. C. Rahn, D. Y. Yan, J. Jiang, M. Bristow, P. Reiss, J. N. Blandy, Y. F. Guo, Y. G. Shi, T. K. Kim, A. McCollam, S. H. Simon, Y. Chen, A. I. Coldea, and A. T. Boothroyd, Ideal weyl semimetal induced by magnetic exchange, Phys. Rev. B **100**, 201102(R) (2019).

[19] L.-L. Wang, N. H. Jo, B. Kuthanazhi, Y. Wu, R. J. McQueeney, A. Kaminski, and P. C. Canfield, Single pair of Weyl fermions in the half-metallic semimetal $EuCd_2As_2$, Phys. Rev. B **99**, 245147 (2019).

[20] N. H. Jo, B. Kuthanazhi, Y. Wu, E. Timmons, T.-H. Kim, L. Zhou, L.-L. Wang, B. G. Ueland, A. Palasyuk, D. H. Ryan, R. J. McQueeney, K. Lee, B. Schrunk, A. A. Burkov, R. Prozorov, S. L. Bud'ko, A. Kaminski, and P. C. Canfield, Manipulating magnetism in the topological semimetal $EuCd_2As_2$, Phys. Rev. B **101**, 140402(R) (2020).

[21] S. Roychowdhury, M. Yao, K. Samanta, S. Bae, D. Chen, S. Ju, A. Raghavan, N. Kumar, P. Constantinou, S. N. Guin *et al.*, Anomalous hall conductivity and nernst effect of the ideal weyl semimetallic ferromagnet $EuCd_2As_2$, Adv. Sci. **10**, 2207121 (2023).

[22] A. F. May, M. A. McGuire, and B. C. Sales, Effect of eu magnetism on the electronic properties of the candidate dirac material $EuMnBi_2$, Phys. Rev. B **90**, 075109 (2014).

[23] H. Masuda, H. Sakai, M. Tokunaga, Y. Yamasaki, A. Miyake, J. Shiogai, S. Nakamura, S. Awaji, A. Tsukazaki, H. Nakao *et al.*, Quantum hall effect in a bulk antiferromagnet $EuMnBi_2$ with magnetically confined two-dimensional dirac fermions, Sci. Adv. **2**, e1501117 (2016).

[24] R. A. Susilo, W. Deng, J. Feng, A. Wang, N. Kawamura, N. Ishimatsu, S. Kawaguchi, M. Yuan, H. Li, W. Ren, T. Nakagawa, C. Petrovic, and B. Chen, Impacts of pressure to the structural, electronic and magnetic properties of Dirac semimetal $EuMnBi_2$, Phys. Rev. Res. **3**, 043028 (2021).

[25] H. Nishiyama, H. Sakai, K. Nakagawa, N. Hanasaki, S. Ishiwata, H. Masuda, M. Ochi, K. Kuroki, S. Iguchi, T. Sasaki, Y. Ikemoto, T. Moriwaki, K. Ueda, Y. Tokura, and J. Fujioka,

Variation of charge dynamics upon antiferromagnetic transitions in the Dirac semimetal $EuMnBi_2$, Phys. Rev. B **104**, 115111 (2021).

[26] X. Gui, I. Pletikosic, H. Cao, H.-J. Tien, X. Xu, R. Zhong, G. Wang, T.-R. Chang, S. Jia, T. Valla *et al.*, A new magnetic topological quantum material candidate by design, ACS Cent. Sci. **5**, 900 (2019).

[27] G. M. Pierantozzi, A. De Vita, C. Bigi, X. Gui, H.-J. Tien, D. Mondal, F. Mazzola, J. Fujii, I. Vobornik, G. Vinai *et al.*, Evidence of magnetism-induced topological protection in the axion insulator candidate $EuSn_2P_2$, Proc. Natl. Acad. Sci. USA **119**, e2116575119 (2022).

[28] Q. D. Gibson, L. M. Schoop, L. Muechler, L. S. Xie, M. Hirschberger, N. P. Ong, R. Car, and R. J. Cava, Three-dimensional dirac semimetals: Design principles and predictions of new materials, Phys. Rev. B **91**, 205128 (2015).

[29] B. Singh, S. Mardanya, C. Su, H. Lin, A. Agarwal, and A. Bansil, Spin-orbit coupling driven crossover from a starfruitlike nodal semimetal to dirac and weyl semimetal state in CaAuAs, Phys. Rev. B **98**, 085122 (2018).

[30] S. Mardanya, B. Singh, S.-M. Huang, T.-R. Chang, C. Su, H. Lin, A. Agarwal, and A. Bansil, Prediction of threefold fermions in a nearly ideal dirac semimetal BaAgAs, Phys. Rev. Mater. **3**, 071201(R) (2019).

[31] H. Gao, J. W. Venderbos, Y. Kim, and A. M. Rappe, Topological semimetals from first principles, Annu. Rev. Mater. Res. **49**, 153 (2019).

[32] C. K. Barman, C. Mondal, B. Pathak, and A. Alam, Symmetry-driven topological phases in $xAgBi(x = Ba, Sr)$: An ab initio hybrid functional calculation, Phys. Rev. Mater. **4**, 084201 (2020).

[33] K. Nakayama, Z. Wang, D. Takane, S. Souma, Y. Kubota, Y. Nakata, C. Cacho, T. Kim, S. A. Ekahana, M. Shi, M. Kitamura, K. Horiba, H. Kumigashira, T. Takahashi, Y. Ando, and T. Sato, Observation of inverted band structure in the topological dirac semimetal candidate CaAuAs, Phys. Rev. B **102**, 041104(R) (2020).

[34] Z. Hu, J. Koo, Y. Hu, Q. Wang, M. Abeykoon, D. Graf, Y. Liu, H. Lei, J. Ma, M. Shi, B. Yan, and C. Petrovic, Topological dirac semimetal BaAuSb, Phys. Rev. Res. **5**, 013079 (2023).

[35] R. Pöttgen and D. Johrendt, Equiatomic intermetallic europium compounds: syntheses, crystal chemistry, chemical bonding, and physical properties, Chem. Mater. **12**, 875 (2000).

[36] Y. Jin, X.-T. Zeng, X. Feng, X. Du, W. Wu, X.-L. Sheng, Z.-M. Yu, Z. Zhu, and S. A. Yang, Multiple magnetism-controlled topological states in EuAgAs, Phys. Rev. B **104**, 165424 (2021).

[37] C. Tomuschat and H.-U. Schuster, Magnetische eigenschaften der verbindungsreihe EuBX mit B= element der ersten neben- und X= element der fünften hauptgruppe, Z. Anorg. Allg. Chem. **518**, 161 (1984).

[38] T. Kurumaji, T. Nakajima, M. Hirschberger, A. Kikkawa, Y. Yamasaki, H. Sagayama, H. Nakao, Y. Taguchi, T.-h. Arima, and Y. Tokura, Skyrmion lattice with a giant topological hall effect in a frustrated triangular-lattice magnet, Science **365**, 914 (2019).

[39] M. Hirschberger, T. Nakajima, M. Kriener, T. Kurumaji, L. Spitz, S. Gao, A. Kikkawa, Y. Yamasaki, H. Sagayama, H. Nakao, S. Ohira-Kawamura, Y. Taguchi, T.-h. Arima, and Y. Tokura, High-field depinned phase and planar hall effect in the skyrmion host gd$_2$pdsi$_3$, Phys. Rev. B **101**, 220401(R) (2020).

[40] T. Nomoto, T. Koretsune, and R. Arita, Formation Mechanism of the Helical Q Structure in Gd-Based Skyrmion Materials, Phys. Rev. Lett. **125**, 117204 (2020).

[41] J. Bouaziz, E. Mendive-Tapia, S. Blügel, and J. B. Staunton, Fermi-Surface Origin of Skyrmion Lattices in Centrosymmetric Rare-Earth Intermetallics, Phys. Rev. Lett. **128**, 157206 (2022).

[42] J. A. M. Paddison, B. K. Rai, A. F. May, S. Calder, M. B. Stone, M. D. Frontzek, and A. D. Christianson, Magnetic Interactions of the Centrosymmetric Skyrmion Material Gd_2PdSi_3, Phys. Rev. Lett. **129**, 137202 (2022).

[43] F. Tang, M. Frontzek, J. Dshemuchadse, T. Leisegang, M. Zschornak, R. Mietrach, J.-U. Hoffmann, W. Löser, S. Gemming, D. C. Meyer, and M. Loewenhaupt, Crystallographic superstructure in R_2PdSi_3 compounds (R = heavy rare earth), Phys. Rev. B **84**, 104105 (2011).

[44] T. Okubo, S. Chung, and H. Kawamura, Multiple-q States and the Skyrmion Lattice of the Triangular-Lattice Heisenberg Antiferromagnet Under Magnetic Fields, Phys. Rev. Lett. **108**, 017206 (2012).

[45] A. Leonov and M. Mostovoy, Multiply periodic states and isolated skyrmions in an anisotropic frustrated magnet, Nat. Commun. **6**, 8275 (2015).

[46] Z. Wang, Y. Su, S.-Z. Lin, and C. D. Batista, Skyrmion Crystal from RKKY Interaction Mediated by 2D Electron Gas, Phys. Rev. Lett. **124**, 207201 (2020).

[47] Y. Tokura and N. Kanazawa, Magnetic Skyrmion Materials, Chem. Rev. **121**, 2857 (2021).

[48] G. Michels, S. Junk, W. Schlabitz, E. Holland-Moritz, M. Abd-Elmeguid, J. Dunner, and A. Mewis, Final-state effects in divalent Eu pnictides, J. Phys.: Condens. Matter **6**, 1769 (1994).

[49] W. Iha, M. Kakihana, S. Matsuda, F. Honda, Y. Haga, T. Takeuchi, M. Nakashima, Y. Amako, J. Gouchi, Y. Uwatoko *et al.*, Anomalous ferromagnetic ordering in EuCuP, J. Alloys Compd. **788**, 361 (2019).

[50] J. Wang, J. Shen, Y. Wang, T. Liang, X. Wang, R. Zu, S. Zhang, Q. Zeng, E. Liu, and X. Xu, Anisotropic magneto-transport behavior in a hexagonal ferromagnetic EuCuP single crystal, J. Alloys Compd. **947**, 169620 (2023).

[51] H. Takahashi, K. Aono, Y. Nambu, R. Kiyanagi, T. Nomoto, M. Sakano, K. Ishizaka, R. Arita, and S. Ishiwata, Competing spin modulations in the magnetically frustrated semimetal EuCuSb, Phys. Rev. B **102**, 174425 (2020).

[52] J. Tong, J. Parry, Q. Tao, G.-H. Cao, Z.-A. Xu, and H. Zeng, Magnetic properties of EuCuAs single crystal, J. Alloys Compd. **602**, 26 (2014).

[53] X. Zhang, L. Yu, S. von Molnár, Z. Fisk, and P. Xiong, Non-linear Hall Effect as a Signature of Electronic Phase Separation in the Semimetallic Ferromagnet EuB_6, Phys. Rev. Lett. **103**, 106602 (2009).

[54] R. S. Manna, P. Das, M. de Souza, F. Schnelle, M. Lang, J. Müller, S. von Molnár, and Z. Fisk, Lattice Strain Accompanying the Colossal Magnetoresistance Effect in EuB_6, Phys. Rev. Lett. **113**, 067202 (2014).

[55] M. Pohlit, S. Rößler, Y. Ohno, H. Ohno, S. von Molnár, Z. Fisk, J. Müller, and S. Wirth, Evidence for Ferromagnetic Clusters in the Colossal-Magnetoresistance Material EuB_6, Phys. Rev. Lett. **120**, 257201 (2018).

[56] P. C. Canfield, T. Kong, U. S. Kaluarachchi, and N. H. Jo, Use of frit-disc crucibles for routine and exploratory solution growth of single crystalline samples, Philos. Mag. **96**, 84 (2016).

[57] A. F. May, J. Yan, and M. A. McGuire, A practical guide for crystal growth of van der waals layered materials, J. Appl. Phys. **128**, 051101 (2020).

[58] J. Rodríguez-Carvajal, Recent advances in magnetic structure determination by neutron powder diffraction, Phys. B (Amsterdam) **192**, 55 (1993).

[59] D. Martien, M. Williamsen, S. Spagna, R. Black, T. DaPron, T. Hogan, and D. Snow, An ultrasensitive differential capacitive dilatometer, IEEE Trans. Magn. **55**, 1 (2018).

[60] H. Zhang and X. Ke, Neutron scattering and transport studies of quantum materials, Ph.D. thesis, Michigan State University, 2022, https://www.proquest.com/dissertations-theses/neutron-scattering-transport-studies-quantum/docview/2656860300/se-2.

[61] N. Lossau, H. Kierspel, J. Langen, W. Schlabitz, D. Wohlleben, A. Mewis, and C. Sauer, EuPtP: a new mixed valent europium-system, Z. Phys. B **74**, 227 (1989).

[62] G. Michels, C. Huhnt, W. Scharbrodt, W. Schlabitz, E. Holland-Moritz, M. Abd-Elmeguid, H. Micklitz, D. Johrendt, V. Keimes, and A. Mewis, Temperature induced valence instabilities in ternary Eu-pnictides: a comprehensive view, Z. Phys. B **98**, 75 (1995).

[63] T. Mishra, I. Schellenberg, M. Eul, and R. Pöttgen, Structure and properties of EuTSb (T = Cu, Pd, Ag, Pt, Au) and YbIrSb, Z. Kristallogr., **226**, 590 (2011).

[64] M. Bałanda, Ac susceptibility studies of phase transitions and magnetic relaxation: Conventional, molecular and low-dimensional magnets, Acta Phys. Pol. A **124**, 964 (2013).

[65] S. Pakhira, M. A. Tanatar, and D. C. Johnston, Magnetic, thermal, and electronic-transport properties of $EuMg_2Bi_2$ single crystals, Phys. Rev. B **101**, 214407 (2020).

[66] W. R. Meier, J. R. Torres, R. P. Hermann, J. Zhao, B. Lavina, B. C. Sales, and A. F. May, Thermodynamic insights into the intricate magnetic phase diagram of $eual_4$, Phys. Rev. B **106**, 094421 (2022).

[67] T. Kurumaji, M. Gen, S. Kitou, H. Sagayama, A. Ikeda, and T.-h. Arima, Anisotropic magnetotransport properties coupled with spiral spin modulation in a magnetic semimetal EuZnGe, Phys. Rev. Mater. **6**, 094410 (2022).

[68] V. I. Fistul, *Heavily Doped Semiconductors* (Plenum, New York, 1969).

[69] C. Bean and D. Rodbell, Magnetic disorder as a first-order phase transformation, Phys. Rev. **126**, 104 (1962).

[70] P. Bonville, J. Hodges, M. Shirakawa, M. Kasaya, and D. Schmitt, Incommensurate modulated magnetic structure in orthorhombic EuPdSb, Eur. Phys. J. B **21**, 349 (2001).

[71] R. Taylor and J. Farrell, Mössbauer effect of europium metal under pressure, J. Appl. Phys. **61**, 3669 (1987).

[72] G. S. Pomrehn, A. Zevalkink, W. G. Zeier, A. Van De Walle, and G. J. Snyder, Defect-controlled electronic properties in AZn_2Sb_2 zintl phases, Angew. Chem., Int. Ed. **53**, 3422 (2014).

[73] J. Willis, I. Bravić, R. R. Schnepf, K. N. Heinselman, B. Monserrat, T. Unold, A. Zakutayev, D. O. Scanlon, and A. Crovetto, Prediction and realisation of high mobility and degenerate p-type conductivity in CaCuP thin films, Chem. Sci. **13**, 5872 (2022).

[74] R. J. Quinn and J.-W. G. Bos, Promising thermoelectric performance in CaAgP with intrinsic Ag vacancies, Appl. Phys. Lett. **120**, 073903 (2022).